1 INTRODUCTION

The study of the temperature dependence of the optical constants of thin films is essential for advancing materials used in next-generation electronic and quantum devices. This thesis presents a comprehensive investigation of tantalum nitride (TaN) thin films deposited by atomic layer deposition (ALD) on silicon substrates with thermal oxide layers. The work combines theoretical modeling, spectroscopic ellipsometry (SE), and X-ray reflectivity (XRR) measurements to extract the optical constants, film thickness, surface roughness, and temperature-dependent dielectric functions of ALD TaN. The results demonstrate that ALD TaN can function as an insulating tunnel-barrier material suitable for superconducting Josephson junctions in quantum information technologies.

Tantalum nitride is widely recognized for its versatility, semiconducting, or insulating behavior depending on stoichiometry and deposition conditions. In the microelectronics industry, metallic TaN is used as a diffusion barrier between copper and dielectric layers; however, its potential as an insulating tunnel barrier has only recently been explored. In superconducting qubits, such as those based on Josephson junctions, the insulating layer determines both coherence time and device reliability. Conventional Al/AlO_x junctions, though widely used, suffer from uncontrolled oxidation and variability in thickness and stoichiometry. ALD TaN provides a promising alternative: it offers atomic-scale control of film growth, excellent uniformity across 300 mm wafers, and compatibility with existing semiconductor manufacturing platforms.

The primary objective of this thesis is to determine the optical constants and temperature-dependent dielectric function of ALD TaN thin films over a wide spectral and thermal range. Secondary goals include verifying film thickness, roughness, and density through XRR, and correlating these parameters with the optical and structural properties. The study seeks to answer key questions regarding the insulating character of ALD TaN, the effect of temperature on its band gap, and its potential role as a robust tunnel barrier in superconducting quantum circuits.

This thesis is organized into three main chapters following the introduction, each addressing a critical component of the research.

The first main section establishes the theoretical and experimental framework of the work. It begins with the fundamentals of electronic band theory, describing how atomic orbitals in solids form energy bands that govern electrical and optical behavior. Concepts such as the density of states and band gap are discussed to link electronic structure with optical response. The chapter then introduces the principles of spectroscopic ellipsometry, a nondestructive optical technique that measures the change in polarization of reflected light to derive the dielectric function. Detailed descriptions of the instrumentation are provided, as well as the sample preparation and data analysis procedures, including back-surface roughening, ultrasonic cleaning, and multilayer optical modeling. This theoretical foundation enables the accurate extraction of optical constants and temperature-dependent dielectric properties of the TaN films.

The next chapter applies X-ray reflectivity (XRR) to quantitatively determine the TaN and SiO_2 layer thicknesses, densities, and interfacial roughness. Using a PANalytical Empyrean diffractometer and Cu Kα radiation, the reflectivity data were modeled with the X’Pert Reflectivity software. The analysis produced values of approximately 23.5 nm for the TaN layer, 39.7 nm for the SiO_2 layer, and a surface roughness below 0.4 nm, closely matching ellipsometric measurements. The density of TaN was found to be 9.8 g cm^{-3}, consistent with a stoichiometric, high-quality film. The excellent agreement between the XRR model and experimental data validates the optical models used in the following section and confirms the uniformity of the deposited films.

The final section presents the central experimental results of the study. TaN films of nominal thicknesses 13 nm and 25 nm were grown by ALD on Si/SiO_2 substrates and characterized using SE across photon energies ranging from 0.03 eV to 6.5 eV and temperatures between 80 K and 600 K. The measured ellipsometric angles (Ψ, Δ) were modeled using Tauc-Lorentz and Gaussian oscillator functions, yielding a band gap of approximately 1.5–1.8 eV, indicative of an insulating character. No evidence of free-carrier absorption was detected, even at elevated temperatures, confirming the suitability of ALD TaN as a tunnel-barrier material. The optical parameters were consistent across the 300 mm wafer, highlighting the process uniformity achievable through ALD. This section demonstrates that the dielectric function of TaN exhibits only minimal variation with temperature, with a small decrease in band gap from 1.8 eV (at 80 K) to 1.5 eV (at 600 K).

This thesis combines theoretical modeling and precise experimental characterization to clarify the optical constants and thermal behavior of ALD-grown TaN films on 300 mm wafers. The findings establish TaN as an optically insulating, compositionally uniform, and thermally stable material with a moderate band gap suitable for integration into superconducting Josephson junctions. The methodologies and results presented here contribute not only to understanding the intrinsic optical properties of TaN but also to advancing its application in scalable quantum computing and high-performance microelectronic devices.

2 GENERAL THEORY AND METHODS

2.1 Introduction

This chapter presents the theoretical foundations and the experimental methods that form the basis of this research project on the temperature dependence of the optical constants of tantalum nitride (TaN) thin films formed by atomic layer deposition (ALD) on 300 mm wafers. The chapter has several aims: to explain the theoretical concepts behind the electronic band structure of solids, to describe the principles of Spectroscopic Ellipsometry (SE), to outline the instrumentation used in the study, to describe the methods of data analysis, and finally, to present the sample preparation procedures in detail. For tantalum nitride thin films, ellipsometry allows characterization of how the refractive index and extinction coefficient vary with wavelength and temperature. Since TaN is of interest for electronic, optical, and protective applications, understanding its optical constants is essential for device design and for understanding its fundamental electronic structure.

2.2 Electronic Band Structure

2.2.1 Introduction to Band Theory

At the atomic level, each isolated atom possesses discrete energy levels where electrons can exist. When atoms are brought together to form a solid, these discrete levels broaden into energy bands due to the overlap of atomic orbitals and the Pauli exclusion principle, which states that no two electrons can occupy the same quantum state (same set of 4 quantum numbers) [1]. The resulting energy spectrum can be described as a series of allowed energy bands separated by forbidden gaps (band gaps). These bands are the fundamental basis of electronic band structure, determining a material's electrical, optical, and magnetic properties.

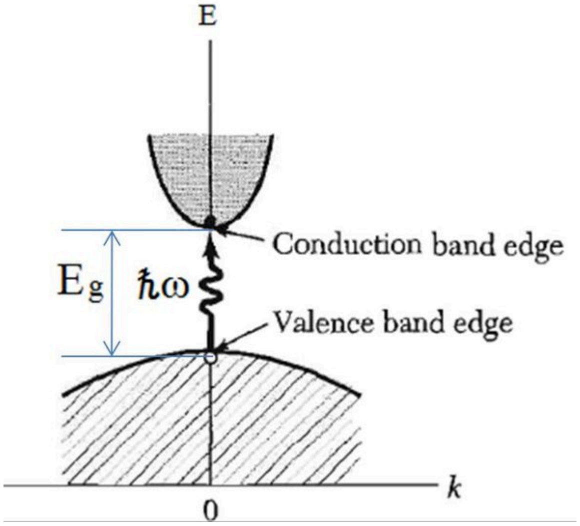

Fig. 1: A band gap is the energy difference between the top of the valence band and the bottom of the conduction band in a solid, with $\hbar\omega$ being the energy required to excite an electron from the valence band to the conduction band. Image retrieved from [2], where it shows the allowed direct optically induced transition of an electron from a valence band state to a conduction band state.

In metals, partially filled bands allow electrons to move freely and conduct electricity. In semiconductors and insulators, the valence and conduction bands are separated by an energy band gap. If the gap is small (on the order of 1-3 eV), the material behaves as a semiconductor; if it is large (greater than about 4 eV), the material behaves as an insulator [3].

2.2.2 Density of States

Another key concept is the density of states (DOS), which specifies the number of electronic states available at a given energy. The DOS plays a central role in determining the electronic, thermal, and optical properties of a material. Optical transitions are allowed between states in the valence band and states in the conduction band if energy and momentum conservation conditions are satisfied. Spectroscopic Ellipsometry (SE) measures the dielectric function, which is a direct consequence of the material's electronic band structure. The key features of the dielectric function are physically rooted in the DOS, meaning SE can be used to probe and confirm a material's electronic structure [4].

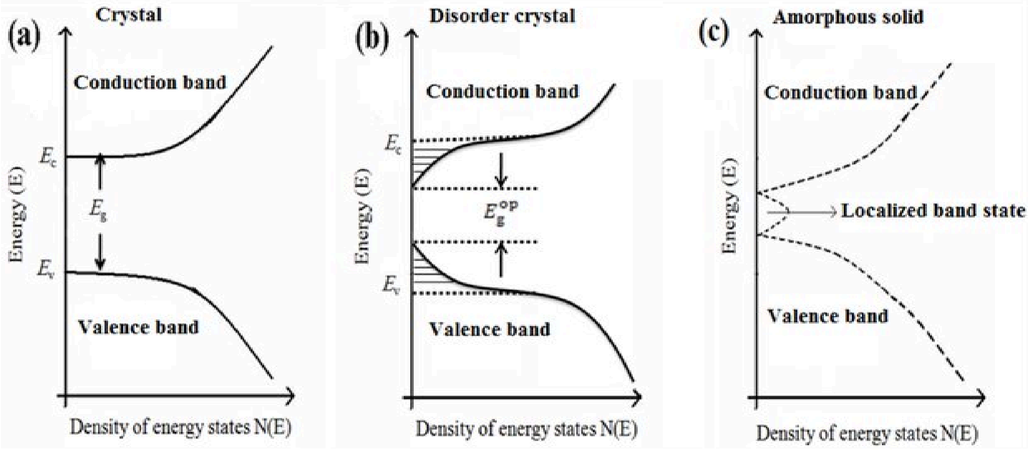

Fig. 2: The density of states is valid only for free electrons, meaning that electrons in a solid are not free, and the density of states is zero inside the band gap. Image retrieved from [2], where it shows a schematic diagram of the band-structure density of states as a function of energy for crystalline (a), disordered (b) and amorphous solid materials (c).

2.2.3 Optical Properties and Band Structure

The optical constants of a material, namely the refractive index n and the extinction coefficient k, are intimately related to its electronic band structure. The refractive index n and the coefficient k are the real and imaginary parts of the complex refractive index $\tilde{n}$:

$$\tilde{n} = n + ik \tag{1}$$

This complex quantity for the refractive index relates to the complex dielectric function $\tilde{\varepsilon}(\omega)$:

$$\tilde{\varepsilon}(\omega) = \varepsilon_1(\omega) + i\varepsilon_2(\omega) = \tilde{n}^2 = (n + ik)^2 \tag{2}$$

Expanding gives:

$$\varepsilon_1 = n^2 - k^2 \tag{3}$$

$$\varepsilon_2 = 2nk \tag{4}$$

So, the optical constants n and k are derived directly from the dielectric response of the material, and this dielectric function $\tilde{\varepsilon}(\omega)$ describes how the material's electrons respond to an electromagnetic field (light) [5]. It has two main components related to the electronic band structure:

1. Interband Transitions — electrons absorb photons and jump between the valence and conduction bands.
2. Intraband (Free Carrier) Transitions — conduction electrons respond to low-energy fields (dominant in metals).

These transitions depend on the energy difference between bands, the density of states, and the transition probabilities (given by the momentum matrix elements). The imaginary part $\varepsilon_2(\omega)$ (and thus k) quantifies how strongly the material absorbs light. It originates from allowed optical transitions between occupied and unoccupied electronic states, while the real part $\varepsilon_1(\omega)$ (and thus n) describes how the light's phase velocity changes, in other words, dispersion.

The extinction coefficient k describes how strongly a material absorbs light at a particular wavelength, and is directly linked to interband electronic transitions (electron transitions between valence and conduction bands). The refractive index n reflects how light propagates within the material, influenced by the polarization response of electrons to the electromagnetic field. Thus, by measuring n(λ) and k(λ), one can reconstruct information about the electronic band structure, such as the optical bandgap, the nature of transitions (direct or indirect) [5], the band curvature and effective masses, and the free carrier concentration (mostly for metals).

By probing a material's response to incident electromagnetic radiation across a wide spectral range, it is possible to infer information about its band structure, band gap, and excitonic effects.

2.3 Theory of Spectroscopic Ellipsometry

2.3.1 Principles of Ellipsometry

Ellipsometry is based on the understanding that light is an electromagnetic wave interacting with materials. Because of this, it provides an optical technique used to determine the dielectric properties (complex refractive index or dielectric function) of thin films [6]. Ellipsometry measures changes in the polarization state of light after reflection from or transmission through a material.

For ellipsometry measurements, the source of light has two linearly polarized waves with electric fields E_s and E_p, which have the same phase and amplitude. The reflection coefficient for p-polarized (electric field oscillating parallel to the plane of incidence) is called r_p, and the reflection coefficient for s-polarized (electric field oscillating perpendicular to the plane of incidence) is called r_s. By reflecting by the sample the relative polarization between E_p and E_s will change, meaning that the light changes to elliptically polarized after interacting with the sample. This change in polarization between the linearly polarized incident beam and the elliptically polarized reflected beam can be quantified by measuring the difference in phase, Δ, and amplitude, Ψ for E_p and E_s [6]. Fresnel's coefficients allow us to measure this difference [7]. Transmission coefficients t_s and t_p are similar to reflection coefficients, although this research focuses only on reflection. The following equations show the reflection coefficients for p- and s-light waves:

$$r_p = \frac{E_{rp}}{E_{ip}} = \frac{n_t cos(\theta_i) - n_i cos(\theta_t)}{n_t cos(\theta_i) + n_i cos(\theta_t)} \tag{5}$$

$$r_s = \frac{E_{rs}}{E_{is}} = \frac{n_i cos(\theta_i) - n_t cos(\theta_t)}{n_i cos(\theta_i) + n_t cos(\theta_t)} \tag{6}$$

Here, the indices r, i and t represent the reflected, incident and transmitted parts of the waves, respectively, between two media of refractive indices $n_1 = n_r = n_i$, and $n_2 = n_t$. These equations consider a plane wave incident on a plane interface at angle of incidence θ_i, a wave reflected at angle $\theta_r = \theta_i$, and a wave transmitted at angle θ_t.

According to energy conservation rules, the sum of reflected light intensity R and transmitted light intensity T must be equal to the total intensity of the incident beam of light. Considering this, the ratio of reflected field amplitudes, $\frac{r_p}{r_s}$, is equivalent to the the tangent of the ellipsometric angle Ψ, which describes the change in amplitude. Ellipsometry characterizes the ratio of these two reflection coefficients, expressed as [7]:

$$\rho = \frac{r_p}{r_s} = tan(\Psi)e^{i\Delta} \tag{7}$$

Here, Ψ is the amplitude ratio and Δ is the phase difference between the p- and s-components. These ellipsometric angles are used to relate to the pseudo-dielectric function.

$$\langle\varepsilon\rangle = sin^2(\theta_i)[1 + tan^2(\theta_i)(\frac{1-\rho}{1+\rho})^2] \tag{8}$$

Once this pseudo-dielectric function is obtained, its experimental data is modeled to extract the dielectric function of the material as a function of wavelength [7]. The optical constants n and k, as well as film thicknesses, can then be extracted by fitting the measured data to appropriate optical models [5]. These values were described in equations (1) and (2).

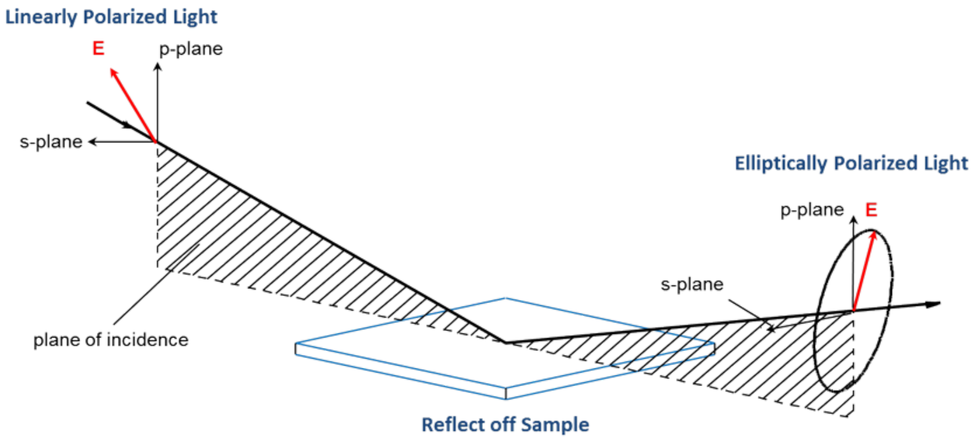

Fig. 3: Diagram describes the change in polarization that occurs when the measurement beam interacts with a sample surface. Image retrieved from J.A. Woollam Ellipsometry FAQ [8].

Something else to mention is that ellipsometry measures the ratio of the reflection coefficients $\frac{r_p}{r_s}$, and since the difference between r_p and r_s is maximized at the Brewster angle, sensitivity for the measurement also increases at this angle. This means that ellipsometry measurement is generally performed at the Brewster angle [9]. The Brewster angle is the specific angle at which the reflected light is completely polarized. When unpolarized light is incident on a flat surface, the reflected light partially polarizes to the plane of the refractive index [10]. This complete polarization at the Brewster angle occurs when the reflected and refracted rays are 90° degrees apart (perpendicular to one another). This can be explained by using Snell's law:

$$n_1 sin\theta_1 = n_2 sin\theta_2 \tag{9}$$

Here, n is the index of refraction of the medium and θ is the angle of the ray from the normal. If we select this incident ray to be at the Brewster angle, θ_B, then:

$$\theta_B + \theta_2 = 90^o \ -> \ \theta_2 = 90^o - \theta_B \tag{10}$$

$$sin\theta_2 = sin(90^o - \theta_B) = sin90^o cos\theta_B - cos90^o sin\theta_B \tag{11}$$

$$sin\theta_2 = cos\theta_B \tag{12}$$

Substituting Eq. (12) into Eq. (9) we have:

$$n_1 sin\theta_B = n_2 cos\theta_B \tag{13}$$

$$tan\theta_B = \frac{n_2}{n_1} \ \Rightarrow \ \theta_B = tan^{-1}(\frac{n_2}{n_1}) \tag{14}$$

This is how the Brewster angle is determined using the index of refraction of the medium [10]. For this project, the Brewster angle and index of refraction of TaN was unknown, so we took ellipsometric measurements at room temperature for incident angles of 50° to 80° to account for the known Brewster angles of Si and SiO_2, which are approximately 75° and 55°, respectively. When the temperature series was performed, we measured only for 70° because that is the only incidence angle that the window on the cryostat allows, which is why the results that are shown in the next chapters, for the most part, only take into consideration the incidence angle of 70^{o}.

2.3.2 Spectroscopic Ellipsometry

In spectroscopic ellipsometry, measurements are taken across a broad wavelength or photon energy range, typically from the ultraviolet (UV) to the infrared (IR). This spectral information provides insight into the electronic transitions, absorption edges, and dispersion behavior of the material [7]. Some advantages of spectroscopic ellipsometry include its high sensitivity to the thin film thicknesses down to sub-nanometer precision, which allows for incredibly accurate measurements; the ability to characterize both n and k; and how it is a non-destructive and contactless procedure that does not damage the samples in any way. Even with all these advantages, ellipsometry does not directly provide optical constants. Instead, it requires model-based analysis where assumptions about layer thickness, roughness, and dielectric functions are made and refined iteratively [7].

Finding the dielectric function of a sample is required for data analysis for spectroscopic ellipsometry, but this may not always be known. In these cases, it is necessary to build dielectric function models that can describe the experimental data. Specific types of dielectric function models work for different spectral regions and characteristics [49]. This project focused on using a Tauc-Lorentz model to describe the ellipsometric data of the TaN layer. A Tauc-Lorentz model is a mathematical formula that describes the optical properties of amorphous materials like semiconductors. It works by combining the Tauc joint density of states model, which accounts for amorphous band tails, with the classical Lorentz oscillator model that describes the absorption peaks in a material [49]. The imaginary part of the dielectric function, ε_2, is defined as

$$\varepsilon_2 = \frac{A En_o C (En - E_g)^2}{(En^2 - En_o^2)^2 + C^2 En^2} \frac{1}{En} \quad \text{for} \quad E_n > E_g \tag{15}$$

where A is the amplitude, En_o is the peak transition energy, E_g is the band gap energy, En is the photon energy at that point, and C is the broadening term for the model. On the other hand, the real part, ε_1, of the dielectric function is derived from ε_2 and is expressed for a total of five parameters: $\varepsilon_1(\infty)$, A, C, En_o, and E_g [49]. Fig. 4 below shows the dielectric function and (n, k) spectra of an amorphous silicon calculated from the Tauc-Lorentz model.

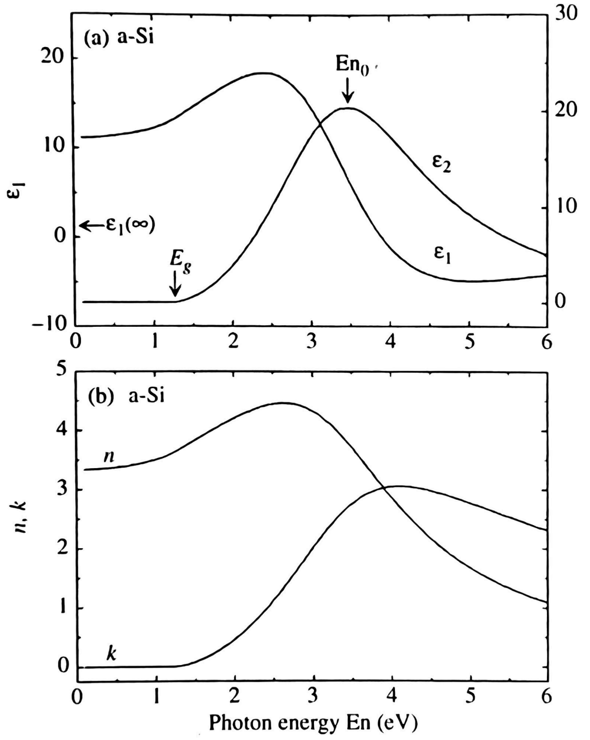

Fig. 4: (top) Dielectric function and (bottom) (n, k) spectra of an amorphous silicon calculated from Tauc-Lorentz model. Image retrieved from [49].

2.4 Instrumentation

2.4.1 IR-VASE MARK II (J.A. Woollam)

The IR-VASE MARK II is an infrared spectroscopic ellipsometer manufactured by J.A. Woollam Co. It is designed to measure optical properties in the infrared region, typically from about 1.7 to 30 µm (microns). This IR ellipsometer has the ability to probe vibrational modes and free carrier absorption in a material, as well as having high accuracy in determining optical constants in the mid-IR region. Additionally, it has compatibility with temperature control stages for studying temperature-dependent effects [11].

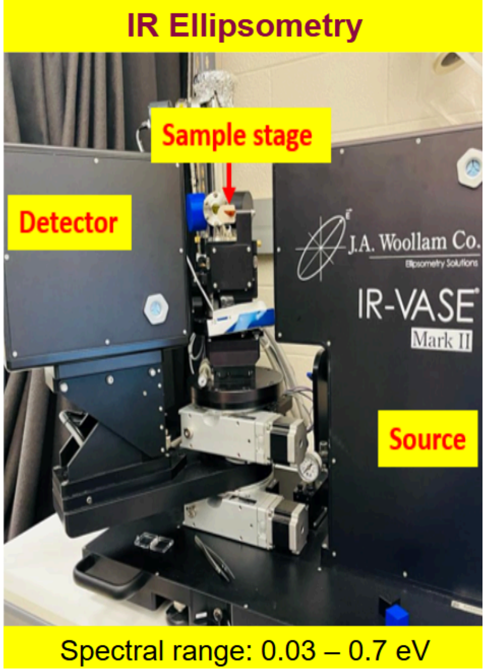

Fig. 5: Image showing the Infrared ellipsometer used for this project, indicating the three main sections of the instrument and the spectral range it measures. The photograph was captured by the research group.

In this project, the IR-VASE was used to measure the infrared optical constants of TaN thin films. Fig. 5 above shows the general setup for this ellipsometer, with the light source on the right side, the sample stage in the middle connected to a vacuum pump to mount the sample, and the detector on the left side.

2.4.2 VASE (J.A. Woollam)

The VASE is a spectroscopic ellipsometer covering the ultraviolet to near-infrared range (typically 193 nm to 2500 nm). It is capable of detecting interband electronic transitions and absorption edges with high sensitivity. This UV ellipsometer has the ability to obtain high spectral resolution across a broad UV-Vis-NIR range (Ultraviolet-Visible-Near Infrared); the sensitivity to measure ultrathin films and multilayer structures; and it also has automated data acquisition with precise angle control [12].

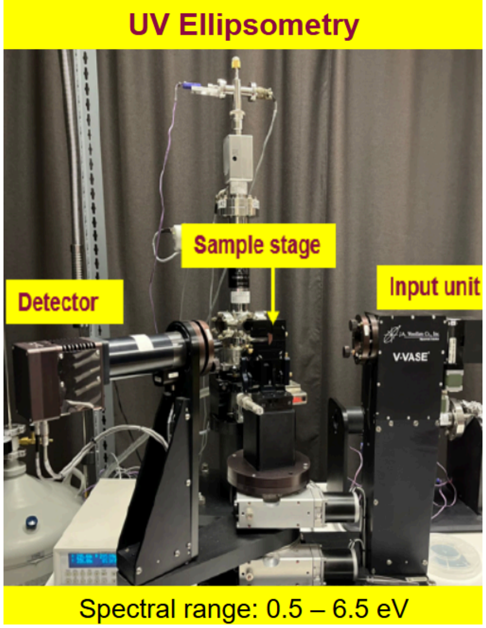

Fig. 6: Image showing the UV ellipsometer used for this project, indicating the three main sections of the instrument and its spectral range. The photograph was captured by the research group.

In this study, the VASE was employed to measure the optical response of TaN in the UV and visible regions. Fig. 6 above shows the general setup for this ellipsometer, with the light source coming out of the right side in the input unit, the sample stage in the middle connected to a vacuum pump to mount the sample, and the detector on the left side.

2.4.3 Lakeshore Janis ST-400 ultrahigh vacuum cryostat

The Lake Shore Janis ST-400 is a compact ultrahigh vacuum cryostat that provides precise temperature control down to ~10 K with optical access for techniques like ellipsometry and spectroscopy. Its UHV design minimizes contamination, and its window ports enable broad spectral measurements, making it ideal for studying the temperature-dependent optical properties of thin films and surfaces [13].

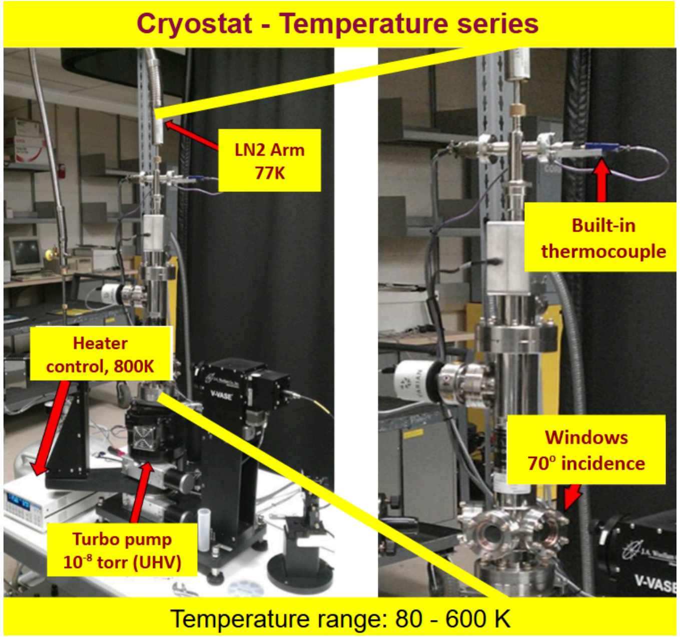

Fig. 7: Image showing the cryostat used for this project, indicating the five main sections of the instrument and the temperature range we measured. The photograph was captured by the research group.

In this study, the UHV cryostat was employed to obtain a temperature series from 80 K to 600 K to study the change in optical constants of TaN in the UV and visible regions.

2.4.4 W-VASE Software (J.A. Woollam)

The W-VASE software, also developed by J.A. Woollam, is used to control the ellipsometers, acquire raw data, and perform model-based analysis. It allows for building multilayer optical models, applying parametrized dispersion models such as Cauchy, Tauc-Lorentz, and Drude-Lorentz oscillators, and has an iterative regression fitting of experimental Ψ and Δ spectra [14].

The software is integral for translating raw ellipsometric measurements into meaningful material parameters such as layer thickness, refractive index, extinction coefficient, and dielectric function.

2.5 Data Analysis Methods

2.5.1 Workflow Overview

Data analysis in this project followed a structured workflow:

1. Acquire Ψ and Δ spectra from both the IR-VASE and VASE instruments using W-VASE software.
2. Import the measured data into W-VASE for initial model fitting and parameter extraction.
3. Once the best model was created following the ε_1 and ε_2 data, export processed data to Microsoft Excel for tabular organization and for the expression of graph points.
4. Use OriginPro to generate publication-quality plots.

2.5.2 W-VASE Analysis

Within W-VASE, models of the multilayer structures were built based on the known sample configurations (substrate, oxide, and TaN layers). Dispersion functions were applied to represent the optical behavior of each layer. Model parameters were adjusted using regression analysis to minimize the mean squared error between experimental data and model.

2.5.3 Excel Usage

Excel was primarily used for numerical organization, quick visualization, and storage of extracted data points. It provided a convenient environment to manipulate raw values into more usable formats, particularly before final graphing.

2.5.4 OriginPro Plotting

OriginPro was employed to create graphs with professional-level clarity. It allowed multi-dataset plotting, curve fitting, and annotation of figures. Graphs generated included the pseudo-dielectric function, the dielectric function, and the Ψ and Δ functions versus wavelength or photon energy, as well as temperature-dependent plots of optical constants.

2.6 Sample Preparation Methods

2.6.1 Overview

A total of 11 samples of 1 inch x 1 inch were prepared from the center, middle, and edge sections of 300 mm wafers. The TaN surface layers were deposited using ALD on top of SiO_2 grown on a Si substrate. This technique ensures conformal, uniform thin films with atomic-level thickness control, making it particularly well suited for preparing reference-quality optical samples. Our preparation process needs to ensure clean surfaces and minimized back-side reflections during ellipsometry measurements, as described below.

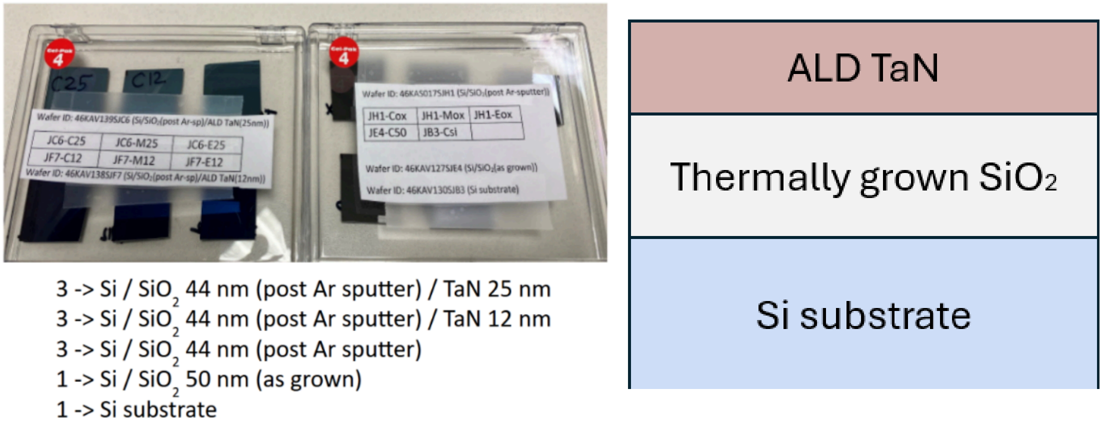

Fig. 8: (top left) Image shows the 11 samples used for this project, and labeled with specific codes describing their characteristics. The photograph was captured by the research group. (bottom left) Shows the layers for each of the samples. (right) Shows a diagram of how the TaN samples are structured with the Si substrate, SiO_2, and TaN.

2.6.2 Back-Side Reflection Removal

To prevent unwanted optical interference from reflections on the back side of the samples, a sandblasting gun was used. Aluminum oxide dust with a 220-grit size was applied to roughen the back surfaces. This treatment effectively eliminated specular reflections from the back surface while leaving the front surfaces intact, leaving the samples to be only 1-side polished.

Fig. 9: Image shows the aluminum oxide (top left), sandblaster (bottom left), and the change in reflection before and after sandblasting the sample. The photographs were captured by the research group.

Fig. 9 above shows how a star was drawn on the back surface of the sample using a black marker. After the sandblaster was used, the star disappeared. This method was used to ensure a thorough use of the sandblaster to block backside reflections.

2.6.3 Cleaning Process

Each sample was cleaned using water (for 15 minutes) and isopropanol (for an additional 15 minutes) inside an ultrasonic cleaner. The ultrasonic waves assisted in removing particulate contamination and surface residues, ensuring a high-quality optical surface for ellipsometry.

Fig. 10: Ultrasonic cleaner used for cleaning the samples. The photograph was captured by the research group.

2.7 Conclusion

This chapter has outlined the general theoretical framework and methods employed in this thesis. The electronic band structure of solids provides the foundation for understanding the optical response of materials, while spectroscopic ellipsometry offers a powerful means of experimentally probing these optical constants across broad spectral ranges.

The instrumentation used, IR-VASE and VASE ellipsometers controlled via W-VASE software, enabled precise measurements. Data was further organized in Excel and presented graphically using OriginPro.

Careful sample preparation was performed to ensure reliable measurements, including ultrasonic cleaning and sandblasting to remove back-side reflections. This project used a set of 11 samples with different configurations of TaN and SiO_2 layers on Si substrates prepared by ALD.

Together, these theoretical and methodological elements form the basis for the investigation of the optical constants and temperature dependence of tantalum nitride thin films, presented in the following chapters.

3 MEASUREMENT OF TANTALUM NITRIDE ON Si/SiO_2 USING X-RAY REFLECTANCE

Aaron Lopez Gonzalez[1], Carlos Armenta[1], Stefan Zollner[1], Ekta Bhatia[2], Tuan Vo[2], and Satyavolu Papa Rao[2]

[1]Department of Physics, New Mexico State University, Las Cruces, NM, USA

[2]NY CREATES, Albany, NY, USA

ABSTRACT

Metallic tantalum nitride (TaN) is typically used to separate layers between copper and dielectric insulator films deposited on top of silicon wafers to create integrated circuits, but it can also form insulating films. This deposition can be done through atomic layer deposition (ALD), where the substrate is exposed to specific reactants inserted in the growth chamber through a series of pulses until the desired deposited layer thickness is reached. We have films of tantalum nitride formed on top of 300 mm wide Si/SiO_2 wafers by atomic layer deposition, and the main purpose of this project is to perform X-Ray Reflectance (XRR) on these thin films to determine the thicknesses of the TaN and SiO_2 layers, as well as their density and the films' surface roughness. XRR is an elastic and specular technique in surface spectroscopy, which means that its angle of reflection is always equal to its angle of incidence, where both angles are measured relative to the surface. Here, the energy of the incident particle equals the energy of the scattered particle, and the intensity of the reflected beam relative to the refracted beam depends on the electron density and angle.

3.1 Introduction

X-Ray Reflectivity (XRR) is an analytical technique used to investigate thin films, structures, and interfaces by exploiting the effect of reflection of X-rays. This technique allows for the characterization of single and multi-layer structures in semiconducting materials, such as the one used for this experiment. The basic idea behind this technique is to reflect a beam of X-rays from a flat surface and measure the intensity of rays reflected in the specular direction, which simply refers to the opposite side of the normal to the surface than the incident beam [15].

For specular reflectivity techniques, the incident and reflected angles are equal. This reflection must occur around the critical angle, which is the angle of incidence below which X-rays undergo total external reflection from a material's surface. This is because the refractive index is very nearly unity over much of the X-ray region, and the Fresnel equations (like Eqs. (5) and (6)) show us that the reflection coefficients for X-rays will only be appreciable at very small angles (which are referred to as "grazing angles") [15].

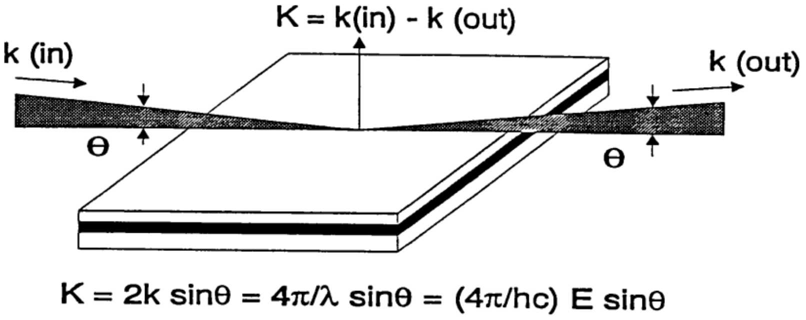

Fig. 11: Scattering geometry for specular reflection. The scattering vector, K, is normal to the surface plane. Image retrieved from [15].

According to Snell's law, x-rays reflect towards the opposite side of the normal of the sample, as seen in Fig. 11. Considering this, the index of refraction of the sample will be:

$$n = 1 - \delta + i\beta \tag{16}$$

In Eq. (16), β represents the absorption of the element (imaginary part) and δ represents the dielectric polarization (real part) [16]. The sign of β depends on the convention used to define the propagation of the electric field. While most engineering textbooks would represent it as negative, we physicists use the convention $exp[i(\omega t + kr)]$ [17].

The values β and δ depend on the electron density, ρ_e, and the mass density, μ, of the element. If we also consider δ in terms of wavelength λ, we end up with the following [16]:

$$\delta = \frac{r_e}{2\pi}\lambda^2\rho_e = \frac{N_A Z r_e \mu}{2\pi A}\lambda^2 \tag{17}$$

In Eq. (17), N_A represents the Avogadro constant (6.02214076×10^{23} mol^{-1}), r_e is the classical radius of the electron ($2.813 \text{ x } 10^{-6}$ nm), A is the mass of the element, Z is the atomic number.

Another important thing to look for whenever doing XRR is the critical angle, which is the angle where the rays are refracted parallel to the interface of air and material. This definition reduces Snell's law to $cos\theta_{crit} = n = 1 - \delta$. After Taylor expansion, we obtain the following expression [17]:

$$\theta_{crit} \approx \sqrt{2\delta} \tag{18}$$

This is the main equation needed to calculate the critical angle. Below the critical angle, we can see the maximum intensity and reflectivity. At the critical angle, we see the reflectivity halved. Above this angle, X-rays start to penetrate the sample, and if the rays encounter a surface with a different index of refraction (this being a layer made of a different material/density/index), they will reflect with a different intensity [17]. This also means that, for angles less than the critical angle, X-rays are totally externally reflected and do not penetrate the sample.

Because of the continuous reflection of these rays by the sample and its various layers with different indices of refraction, interference between the reflected rays will start to appear. If the reflected rays interfere constructively, the intensity detected will be greater, and if the rays interfere destructively, then the intensity will drop [18]. Since this has a cyclic behavior, the reflected intensity of a sample will show oscillations when visualized in $\log_{10}$ for the vertical axis as a function of angle. These oscillations in the XRR spectrum are known as *Kiessig fringes* [19]. An example of a specular XRR pattern is shown in Fig. 12.

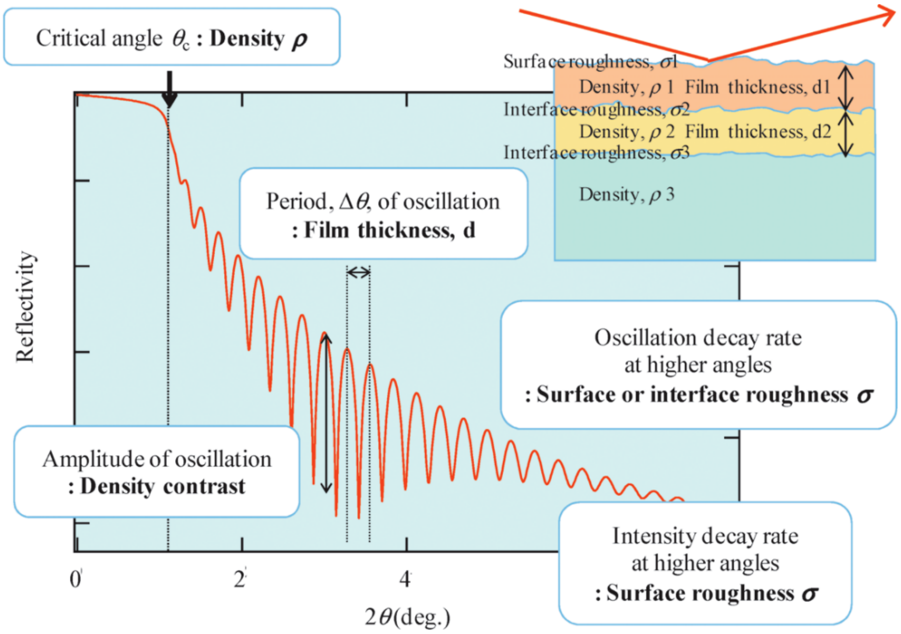

Fig. 12: Information provided by X-ray reflectivity profile. Image retrieved from [18].

Now we know that oscillations are part of the XRR pattern, but this also means that they should have a specific frequency. The way we can relate the frequency of these oscillations to the thickness is by looking at the period completed by each oscillation. Each oscillation will appear at integers of the wavelength λ. If we express this in reciprocal space, then the thickness of the layer will be given by the following equation [20]:

$$T = \frac{\lambda}{2 * \Delta\theta} = \frac{2\pi}{\Delta Q} \tag{19}$$

where $\Delta\theta$ is the spacing between the interference fringes and ΔQ is the spacing but in the reciprocal space dimension. Basically, they represent how distanced are the fringes from one another - the periodicity.

The equations for the index of refraction, and the thickness of the layer were given, but there is still another important component that is part of the values we can find with XRR, and that is the surface roughness of each layer. Fig. 12 shows the slope that the XRR pattern follows, and it labels it as "roughness". This is because the slope of the fringes will be correlated to the roughness of the layer. This surface roughness determines the overall decay rate of the reflecitvity curve as the scattering angle increases because the missing intensity of the specularly reflected beam is scattered into other directions. Similarly, the amplitude of oscillations will be correlated to the density contrast, and the critical angle relates to the density of the material, as explained for Eq. (18) [20].

Something very important in XRR is that this method is related to electron density differences at interfaces. Here, the materials can sometimes be amorphous, which means no long-range order; they can also be crystalline, liquid, and even then, the interference fringes are still present because there is a change in refractive index across interfaces. By modeling the experimental XRR curve, it is possible to obtain a quantitative electron density profile of the sample as a function of depth, which can reveal the electron density of each layer and the sharpness of the interfaces between layers.

In a typical XRR experiment, the incident angle, θ, is equal to the exit angle, θ, which is why 2θ is the total scattering angle. Since XRR focuses on specular reflection, the scattering vector, q, is defined by the difference between the scattered X-ray wave vector, k_f, and the incident X-ray wave vector, k_i, as seen in the following equation:

$$q = k_f - k_i \tag{20}$$

Where the magnitude of the scattering vector is a function of the X-ray wavelength, λ (approximately equal to 1.54 Å because we use copper $K\alpha$ radiation), and the scattering angle, 2θ:

$$q = q_z = \frac{4\pi}{\lambda} sin\theta \tag{21}$$

Because XRR focuses on specular reflection with the incident and exit angle being equal, the scattering vector is divided in two components q_x and q_z, with $q_x = 0$ because the symmetry of the setup makes the in-plane (parallel) component to the sample surface equal to 0, and q_z being the momentum transfer that is perpendicular to the sample surface. Therefore, reflectivity measurement is plotted as a function of q_z for data analysis.

Equation (21) can be used to convert the scattering angle to the reciprocal space coordinate, q_z, when the intensity peak of an oscillation is known for a specific angle of 2θ. Plotting the X-ray reflectivity intensity as a function of q_z gives the material's electron density. The electron density is a key feature of the XRR curve that corresponds to specific properties of the thin film.

The critical angle shown in equation (18) can also be converted to the reciprocal space coordinate, which in this specific case is expressed as q_c. This critical angle is directly related to the average electron density of the material because q_c depends on the elemental composition and packing density of the film.

3.2 Methods

The sample analyzed for this project was Si as the main substrate with SiO_2 and TaN. This thin film was obtained from the center section of a 300 mm wafer, and was originally 2-side polished. To roughen the sample and avoid backside reflections, it was sandblasted using a mid-size air compressor, a sandblaster, and aluminum oxide with a 220-grit. Once the sample was roughened, it was cleaned using isopropanol inside an ultrasonic cleaner.

The primary instrument for this experiment is the Panalytical Empyrean Powder Diffractometer [21], which determines various surfaces and layers of thin films by using incident Cu characteristic K_α X-rays. The setup used for this XRR experiment consisted of:

Incident beam optics:

- Hybrid monochromator 2xGe(200) for Cu
- Fixed divergence slit of 1/32º
- Fixed mask of 10 mm

Diffracted beam optics:

- Parallel plate collimator slit

- Parallel plate collimator of 0.27°
- Soller slits 0.04 rad.
- Ni beam attenuator of 0.125 mm
- Xe proportional count detector

To determine the range of 2θ to be used, a fast scan was performed on the sample. This fast scan lasted around 1 hour, and it showed that a range of 0° to 5° was the best option for this measurement since the first range selected (0° to 3°) was not displaying the entire XRR pattern. Once we knew the range of 2θ we needed to use, we started a long scan that lasted approximately 4.5 hours. It is important to visualize the whole XRR pattern because the intensity decay rate provides the information needed to calculate the surface roughness of the layer. The obtained data from the long scan is shown in Fig. 13:

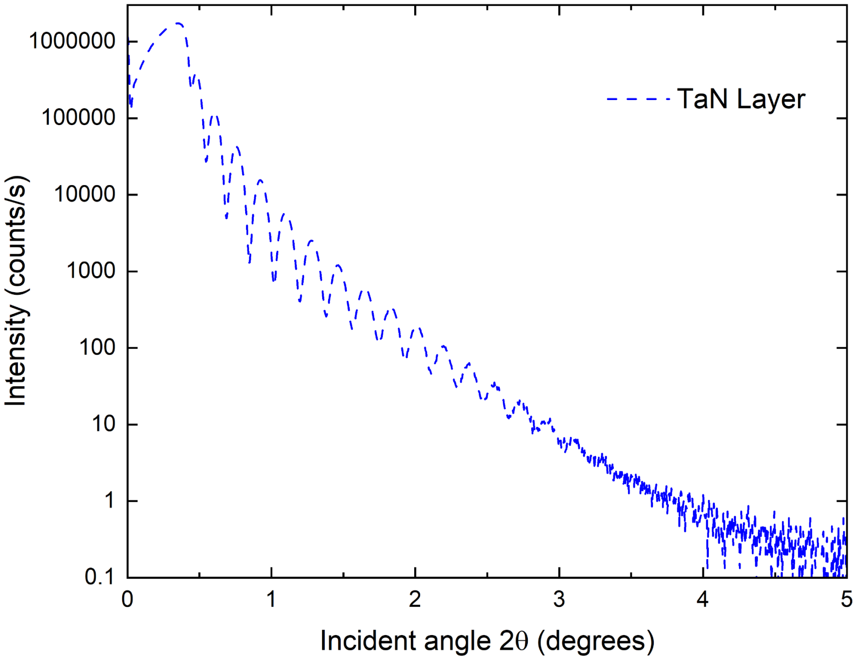

Fig. 13: Collected XRR data for TaN thin film in terms of intensity.

Before modelling our data through software, an estimated thickness and density were calculated for the samples. The peaks of the fringes were measured for the range of 0^{o} to 1.2^{o}. The values shown in the Table 1 were manually selected from all the data points obtained from this measurement. The value for the critical angle was found by identifying the first maximum of the reflected intensity, then dividing in half its intensity (as per Eq. 18), and finally looking for an angle that corresponds to the intensity that matches the closest to what we calculated [18, 20].

Critical angle (deg)		Intensity (counts/s)	
0.415		873340.4	
Angle peak (deg)	Angle valley (deg)	Intensity (counts/s)	
	0.445		232286.1
0.475		396213.1	
	0.545		27097.6
0.605		121914.4	
	0.69		4966.5
0.755		42754.2	
	0.845		1290.5
0.925		15486.1	
	1.02		645.4
1.095		5863.1	
	1.2		404.6

Table 1: This table shows the intensity value at the critical angle, and the intensity values for the next 5 oscillations, including their values at the peaks of the oscillations and at the valleys (minimum).

The data obtained in Table 1 was used to calculate the q_z values for the critical angle and the first five peaks after it, following equation (21). These values are shown in Table 2 below:

	θ (deg)	q (nm^{-1})
Critical angle	0.415	32.900 $\pm$ 0.01
First peak	0.475	37.319 $\pm$ 0.01
Second peak	0.605	46.411 $\pm$ 0.01
Third peak	0.755	55.919 $\pm$ 0.01
Fourth peak	0.925	65.167 $\pm$ 0.01
Fifth peak	1.095	72.536 $\pm$ 0.01

Table 2: Converted values of scattering angles into reciprocal space coordinate q. The errors in the calculated q values are due to the rounding of the results to four significant figures.

Equation (19) shows that we need to find the spacing between the fringes to calculate the layer thickness. Table 3 below shows the values calculated for the distance between the peaks of the first five oscillations:

Oscillations	Δθ (deg)	ΔQ (nm^{-1})
1st-2nd peak	0.130	9.092 $\pm$ 0.014
2nd-3rd peak	0.150	9.508 $\pm$ 0.014
3rd-4th peak	0.170	9.248 $\pm$ 0.014
4th-5th peak	0.170	7.369 $\pm$ 0.014
Average spacing	0.155	8.804 $\pm$ 0.014

Table 3: Δθ of the first 4 oscillations in the XRR pattern, and the average spacing.

Using software *X'Pert Reflectivity*, a model was built and fitted by trying different layers and varying the initial parameters to fit the data. Since the software did not have a layer for TaN, we had to create it from scratch, editing a layer and adding Tantalum and Nitrogen with the default settings for each of them. After doing this, we added the Si substrate, then the SiO_2 layer with a thickness of around 40 nm (which is what we thought was the thickness of the oxide layer), and finally the TaN layer with a thickness of 25 nm (also because of an initial assumption we had).

3.3 Results

By rearranging equations (17) and (18) to solve for the electron density of the material, ρ_e, and considering the critical angle in radians (0.00724), ρ_e was calculated as: $3.7919 \pm 0.0029 * 10^{24}\, cm^{-3}$, considering the value for δ as $2.621 \pm 0.002 * 10^{-5}$. Knowing the value for the electron density, the mass density of the material was calculated using equation (17), and taking into consideration that the molar mass, A, of TaN is $194.955 \pm 0.00022 \frac{g}{mol}$, and the sum of its atomic number is 80 (73 for Ta + 7 for N). Solving equation (17) for the mass density of the TaN layer, we obtained a value of $9.9643 \pm 0.0076 \frac{g}{cm^3}$. Once this mass density was obtained from the experimental data, the layer thickness was also calculated. The angular separation was measured and shown in Table 3, where the average spacing between the first four oscillations was 0.155° or 0.002705 radians. Following equation (19), the thickness for the TaN layer was calculated to be 28.52 ± 0.02 nm. While roughness causes the decay of the XRR signal at higher angles, the exact rate of decay is dependent on a complex interplay of other factor apart from the slope, so it requires a specialized software for analysis. This is why the roughness of the layer was not calculated directly from the experimental data. Roughness is found by using a fitting program to match the experimental data to a theoretical model that incorporates roughness parameters. The results from this model can be seen in Fig. 14.

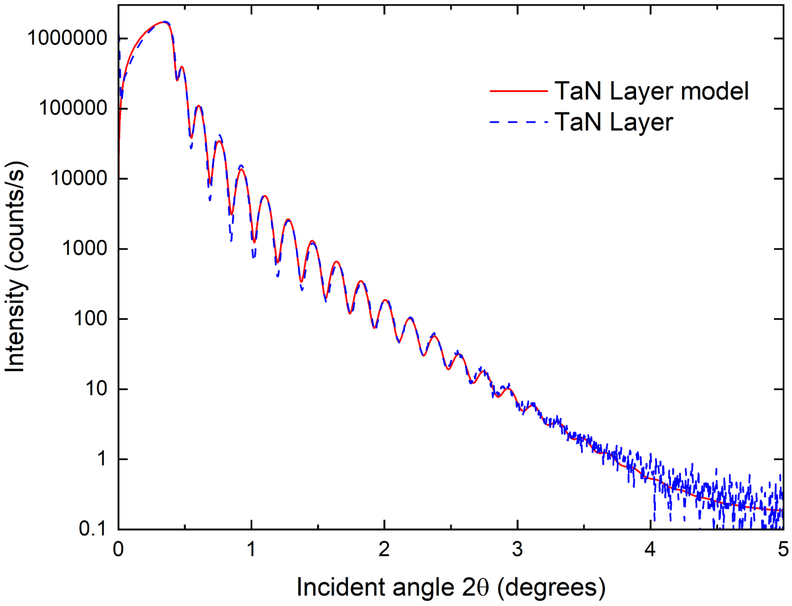

Fig. 14: TaN raw data and model from XRR.

Once the model was executed, it took approximately 7 seconds to adjust to the experimentally obtained XRR pattern. For this model, at first we only allowed the roughnesses to vary, then we also allowed the thicknesses of TaN and the oxide layer, and finally we allowed the TaN density to vary. This model ended up giving us a more accurate idea of the thicknesses that each layer had (note: the thickness of Si shown in Table 4 is not considered since it is the substrate).

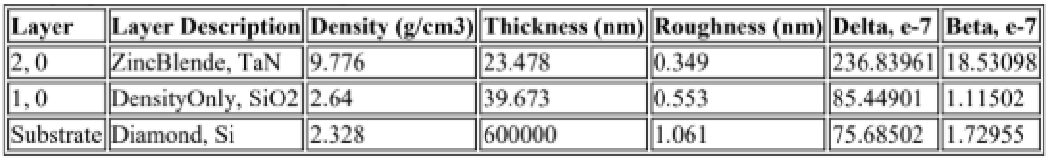

Layer	Layer Description	Density (g/cm3)	Thickness (nm)	Roughness (nm)	Delta, e-7	Beta, e-7
2, 0	ZincBlende, TaN	9.776	23.478	0.349	236.83961	18.53098
1, 0	DensityOnly, SiO2	2.64	39.673	0.553	85.44901	1.11502
Substrate	Diamond, Si	2.328	600000	1.061	75.68502	1.72955

Table 4: Sample parameters after fitting the model.

The results for the model built, seen in table 4, show a TaN layer density of $9.776\ \frac{g}{cm^3}$, a thickness of 23.478 nm, and a roughness of 0.349 nm. Although the X'Pert Reflectivity software did not allow us to visualize the error bars for these measurements, manual variations were made on the model to observe any major changes that happened to the fit of the model to determine the uncertainties of these values.

	Density (g/cm^3)	Thickness (nm)	Roughness (nm)
ZincBlende, TaN	9.776 ± 0.005	23.478 ± 0.005	0.349 ± 0.005

Table 5: Sample parameters with errors after fitting the model.

After making sure the model accurately described the experimental data, we started working on the analysis of this XRR pattern, as shown in Fig. 15.

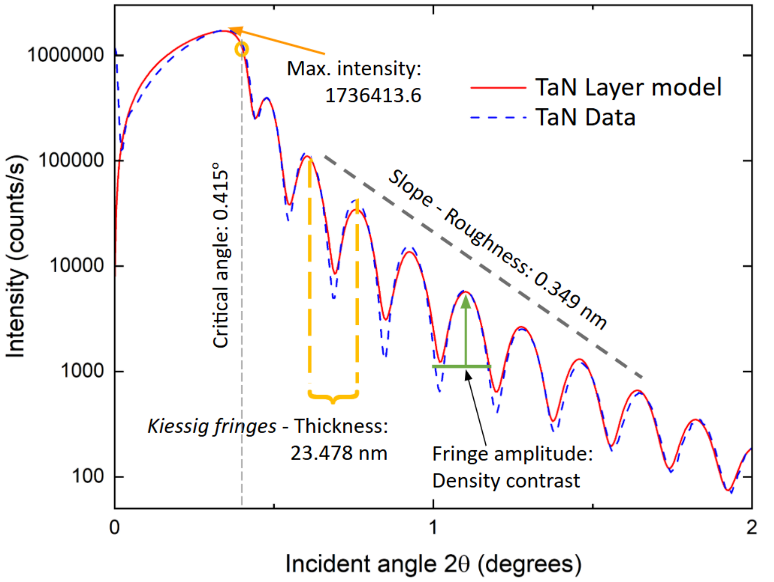

Fig. 15: Close-up of the peaks of the TaN raw data and model from XRR, with various components labeled.

Fig. 15 shows all the different components that an XRR pattern should display, including the position and value of the critical angle, the maximum intensity (which relates to the density), the found thickness of the layer, and the layer roughness for TaN.

The beam divergence used in the fit was 0.004°. The background (counts/s) was 0.17. The final intensity (counts/s) was 3137617, and the thicknesses found for TaN and SiO_2 are 23.478 nm and 39.673 nm, respectively.

	Density (g/cm^3)	Thickness (nm)	Roughness (nm)
TaN, experimental	9.9643 ± 0.0076	28.52 ± 0.02	-----
TaN, model	9.776 ± 0.005	23.478 ± 0.005	0.349 ± 0.005

Table 6: Comparison of experimentally obtained results and model based results for sample parameters using XRR.

The results obtained from the model are in the same order as those calculated directly from the experimentally obtained data. For the density of the layer, there is a difference of 0.1883 ± 0.009 g/cm^3, which shows a good coherence of the model to describe the experimental data. For the thickness of the layer there is a difference of 5.042 ± 0.021 nm, which represents a not too large but still noticeable variation in layer thickness that can be attributed to the limited use of fringes when manually calculating the average fringe spacing. The model takes into consideration all the noticeable fringes of the pattern and takes the average of them all, while the experimental data we calculated only considered the first 5 oscillations. This limitation in the amount of oscillations considered could explain the 5 nm difference in the layer thickness calculation.

Note: Although this thesis includes this XRR chapter before the ellipsometric measurements, the work done with XRR was performed at the very end. The thicknesses used for the next chapter do not align with what was found in this chapter because, for the ellipsometry analysis, we worked with thickness values provided by a previous XRR analysis.

3.4 Conclusion

The X-Ray Reflectance analysis of the TaN thin film based on Si/SiO_2 showed a model that aligned very closely with the experimentally obtained XRR pattern, with values for the critical angle of 0.415^o, the TaN layer thickness of 23.478 nm (which align with the expected thickness for this sample), a surface roughness of 0.349 nm, and a layer density of 9.776 g/cm^3. Although the experimentally obtained values for thickness and layer density were different, they still followed what we expected from this TaN layer. Sources of error considered for some of the values were the inability of the software to show error bars, which led to an “eye-balling” of the errors for the model results; rounding considerations for the intensities and reciprocal space coordinates; and error propagation when solving for electron density, mass density, fringe spacing and layer thickness. This work also considered the possibility for systematic errors, especially since this measurement was only done once. The angle range of 0.7^o to 1.7^o of the XRR pattern shows a slight difference in amplitude between the experimental data and the model, which can be attributed to the sample having more than one layer. This is something that can be worked on in a future experiment, trying to fit a model, and adding more layers for TaN. For now, the model built for this XRR pattern is greatly satisfactory in accurately describing the experimental data.

4 TEMPERATURE-DEPENDENT DIELECTRIC FUNCTION OF TANTALUM NITRIDE FORMED BY ATOMIC LAYER DEPOSITION FOR TUNNEL BARRIERS IN JOSEPHSON JUNCTIONS

Ekta Bhatia,[1] Aaron Lopez Gonzalez,[2] Yoshitha Hettige,[2] Sandra Schujman,[1] Kevin Musick,[1] Thomas Murray,[1] Kim Kisslinger,[3] Chenyu Zhou[3], Mingzhao Liu,[3] Satyavolu S. Papa Rao,[1] and Stefan Zollner[2]

[1]*NY CREATES, Albany, NY, USA*

[2]*Department of Physics, New Mexico State University, Las Cruces, NM, USA*

[3]*Brookhaven National Laboratory, Upton, NY*

Abstract

We report the dielectric functions of insulating tantalum nitride (TaN) films, deposited using atomic layer deposition (ALD) on 300 mm Si/SiO_2 substrates, to demonstrate their suitability as tunnel barriers in tantalum-based Josephson junctions for superconducting quantum circuits. The temperature-dependent ellipsometric angles were measured using ALD TaN films with nominal thicknesses of 13 nm and 23 nm at an incidence angle of 70°, across photon energy ranges of 0.03 eV to 0.7 eV (at 80 K, 190 K, and 300 K) and 0.5 eV to 6.5 eV (80 K, 190 K, 300 K and 600 K). This data was used to develop a dispersion model for insulating ALD TaN films that incorporates a Tauc-Lorentz oscillator with a band gap of 1.5-1.8 eV to model the interband optical transitions. The extracted dielectric function of ALD TaN films shows an insulating character (mid-infrared transparency) at the various temperatures and both film thicknesses tested. ALD TaN does not exhibit infrared absorption due to free carriers (typically seen for

metals), even at elevated temperatures, demonstrating its insulating nature, which is a required characteristic for the tunnel barrier of the Josephson junction in quantum applications. The results of transmission electron microscopy, including selected area electron diffraction, and X-ray diffraction are also discussed. X-ray photoelectron spectroscopy analysis establishes the composition as N/Ta = 1.2 at different locations across the wafer, indicative of the across-wafer uniformity of the films. Compared to conventional aluminum oxide barriers, ALD TaN is expected to show improved thermal stability and resistance to aging. The lower band gap of ALD TaN (1.5-1.8 eV), compared to that of aluminum oxide, suggests the possibility of fabricating Josephson junctions with thicker barriers while achieving critical current densities required for qubits, better control of thickness and composition, and reduced defect densities. These characteristics show the potential of ALD TaN as a Josephson junction tunnel barrier that can improve the reliability and performance of superconducting quantum computing circuits.

4.1 Introduction

The development of the field of quantum computing depends on the fabrication of reliable and efficient qubits [22,23]. A Josephson junction (JJ), incorporating a superconductor-insulator-superconductor (S-I-S) trilayer, is an essential building block of superconducting qubits [24, 25, 26]. To date, JJs have been fabricated using Al as the S layer, along with a 1 nm thick AlOx insulator layer formed at room temperature by controlled exposure to oxygen – in some cases the Al/AlO_x/Al stack forming the junction is connected with Nb wiring. Recently, Ta has gained attention as a superconducting material for qubit devices as the coherence time was improved to as high as 300 μs [27] and 500 μs [28] when the material forming the shunt capacitor of the qubit was changed from Nb to Ta. However, these qubits used the traditional Al/AlO$_x$/Al Josephson junctions. Qubits using Al/AlO$_x$ suffer from fabrication-related control issues that result in varying qubit frequencies – causing significant design and process overheads in order to avoid cross-talk between qubits. There have been efforts to replace room-temperature oxidation of Al with ALD Al_2O_3 as the tunnel barrier – though qubit performance using such a tunnel barrier has not been established [29].

Ta-based qubits that are scalable and reliable, and have predictable performance characteristics, can be fabricated using CMOS-compatible processes in state-of-the-art 300 mm wafer scale fabrication equipment. This requires the development of α-Ta electrodes as has been shown in our earlier work on chemical mechanical planarization of α-Ta for superconducting devices [30]. It also requires the development of a tunnel barrier, such as TaN, that is insulating, has excellent intrinsic thermal stability, is resistant to aging during air ambient storage, and whose interface with the electrode material (α-Ta in this study) is stable. Minimal disruption of typical processes [31] in a 300 mm CMOS IC fabrication facility is another highly desirable characteristic for the tunnel barrier.

A TaN tunnel barrier also has the additional advantage that Ta sputtered onto it preferentially forms the α-Ta phase, which has the superconducting transition temperature required for quantum applications [30]. ALD is a deposition technique for growing conformal films with atomic-scale control of deposited thickness, and ALD TaN as a material is known in the CMOS IC industry. Although several materials such as ALD Al_2O_3 [29], sputter-deposited AlN [32], and sputter-deposited TaN [33] have been explored as alternatives to room-temperature oxidation of Al to form Al oxide, there have been no reports on the use of ALD TaN as an insulating barrier in Josephson junctions, other than the work that this group has conducted [34]. Spectroscopic ellipsometry (SE) is a powerful technique to quantify the dielectric characteristics of materials

[35]. Along with SE, the ALD TaN films were characterized by atomic force microscopy (AFM), for morphology, thickness through X-ray reflectometry (XRR) and transmission electron microscopy (TEM) and assessments of crystallinity through X-ray diffraction (XRD) and selected area diffraction (SAD) in the TEM. Stoichiometry and its variation through film depth were analyzed through sputter profiling XPS.

This chapter focuses on the detailed SE measurements of ALD TaN films deposited on 300 mm wafers in a wide temperature range from 80 K to 600 K, in photon energy ranges from 0.03 eV to 0.7 eV for the infrared wavelengths, and from 0.5 eV to 6.5 eV to cover visible and ultraviolet wavelengths. Such ellipsometric data, acquired at a range of different incidence angles, was used to model the dielectric function of the ALD TaN films. We also determined the non-uniformity of thickness, stoichiometry, and band gap across the 300 mm wafer. This work demonstrates the suitability of ALD TaN deposited on Si/SiO$_2$ as a tunnel barrier for Ta-based and Nb-based S-I-S JJs, with the promise of attendant improvements in junction quality and qubit stability.

4.2 Experimental

4.2.1 Sample preparation

A 50 nm thick silicon oxide layer was thermally grown on B-doped Si (100) wafers with a diameter of 300 mm and a nominal resistivity of 0.1 Ωm. ALD TaN films of different thicknesses (nominally 13 nm and 23 nm) were deposited on the silicon oxide layer in a 300 mm cluster tool, using commercially available, proprietary chemistries. A few conditioning wafers were used before the growth of the ALD TaN film in order to ensure the chamber stability in terms of particles on the wafer after deposition [36]. The films were then characterized using in-line

XRR, AFM, and XPS tools. The wafer was cut into coupons for offline measurements such as TEM, sputter-profiling XPS, and SE.

4.2.2 Spectroscopic Ellipsometry set-up

Spectroscopic ellipsometry measurements were performed on samples from the wafer center, mid radius, and edge for two different thicknesses of ALD TaN on thermal oxide of silicon, along with control measurements made of the thermal oxide and the silicon substrate to serve as inputs for modeling the ALD TaN data. A mid-size air compressor was used to blast alumina particles onto the back surface of the samples to roughen them. Aluminum oxide of grit 220 proved to be the best choice for roughening the back surface of these samples, without causing scratches on the front surface, in order to reduce specular reflections of infrared wavelengths from the back surface of the silicon wafer, permitting better data acquisition without depolarization of the reflected beam and easier data modeling. The samples were then cleaned ultrasonically with distilled water and isopropyl alcohol after sandblasting. The spectroscopic ellipsometry measurements were performed on a J. A. Woollam V-VASE rotating-analyzer ellipsometer equipped with a Berek waveplate compensator and a J. A. Woollam Fourier-transform infrared (FTIR) VASE Mark II rotating-compensator ellipsometer [35, 37], as shown in Fig. 16. Temperature-dependent data from 80 K to 600 K were collected inside a Janis ST-400 ultra-high vacuum (UHV) cryostat (with quartz windows on the V-VASE and diamond windows for the IR-VASE), with liquid nitrogen for cooling and a 50 W Pt resistor for heating [35]. Room-temperature spectra were acquired at incidence angles from 50° to 80°, in steps of 5°, and from 0.5 to 6.5 eV with 0.02 eV steps, but temperature-dependent measurements were restricted to an incidence angle of 70°. Measurements were carried out with five positions of the

Berek wave plate compensator and both positive and negative polarizer angles to improve accuracy. We selected a broad range of incidence angles at room temperature because the Brewster angle of SiO_2 (55°) is much smaller than that of Si (75°). We also acquired infrared spectra at the same angles of incidence from 0.03 to 0.70 eV with 8 cm^{-1} resolution and a fixed analyzer (0° and 180°) and polarizer (±45°).

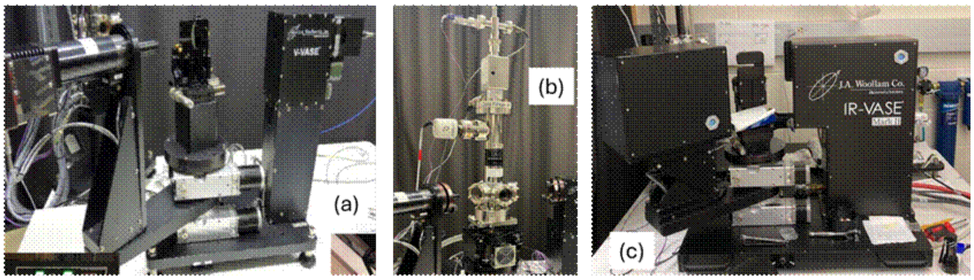

Fig. 16: Spectroscopic ellipsometry set-up: a) J. A. Woollam V-VASE Ellipsometer, b) ultrahigh vacuum cryostat c) J. A. Woollam Fourier-transform infrared ellipsometer.

4.2.3 TEM set-up

TEM analysis was performed on a coupon taken from the mid-radius region of the wafer with a nominal 23 nm ALD TaN film. A carbon layer of 50-60 nm thickness was deposited on each sample to protect the ALD TaN film during the focused ion beam (FIB) preparation of TEM samples. These analyses were performed using a ThermoFisher Titan3 G2 80-300 system. This setup consists of an XFEG electron gun, a monochromator, and a probe spherical aberration corrector. For imaging, the machine was configured in STEM mode, operating at an accelerating voltage of 300 kV and a beam current close to 100 pA. The imaging was done using a 50 µm C2 aperture and 17.9 mrad convergence angle, with simultaneous capture from both bright-field and high angular aperture dark field (HAADF) detectors. This sample was also used for selected area diffraction analyses conducted in the same microscope.

4.2.4 XPS set-up

XPS measurements of the 23 nm ALD TaN film were performed on 3 samples (each 10×5 mm^2), taken from the wafer center, mid-radius, and wafer edge regions. A PHI Quantera Hybrid XPS system was used for these measurements, utilizing an X-ray source with an energy of 1486.6 eV (Al Kα) and a focal spot of 200 μm. The XPS data was collected at take-off angle of 90°. These measurements were performed at a pass energy of 55 eV and utilizing a step increment of 0.05 eV in the chosen binding energy ranges applicable to O1s, N1s, C1s, and Ta4f.

The depth profiles were carried out by sputtering using 2 keV Ar^+ ions in steps, totaling 30-90 s, depending on the sample thickness, and measuring x-ray generated photoelectrons from the center of the crater after each sputter step. The sputtered area was a 3 mm by 3 mm square, while the X-ray beam diameter used is 200 μm.

4.3 Results and Discussion

Fig. 17 shows the ellipsometric angles Ψ and Δ, and the pseudodielectric function (data and model) for a nominally 23 nm thick TaN sample in the center of the wafer at room temperature. $tan(\Psi)$ and Δ represent the amplitude and phase of the complex Fresnel reflectance ratio of p- and s-polarized light for incidence angles varying from 50° to 80° with a step size of 5°. The pseudodielectric function $<\varepsilon>$ is calculated from the ellipsometric angles under the assumption that the sample is a bulk substrate, which ignores the layered structure. The spectral range in the IR from 0.03 to 0.7 eV and in the UV from 0.5 to 6.5 eV were combined in a single data set. There is no indication of free carrier absorption by the ALD TaN film, demonstrating its insulating characteristics and its suitability as a tunnel barrier in Josephson junctions for quantum applications [36]. This contrasts with the free carrier absorption observed in earlier reports on the conductive ALD TaN films for CMOS IC purposes [38]. In the infrared spectral region, $<\varepsilon>$ is dominated by molecular absorption by Si-O vibrations followed by a broad interference fringe between 1 and 2 eV. Since the TaN/SiO$_2$ layer stack is partially transparent, the E_1 peak of the Si substrate is visible in $<\varepsilon>$ near 3.4 eV.

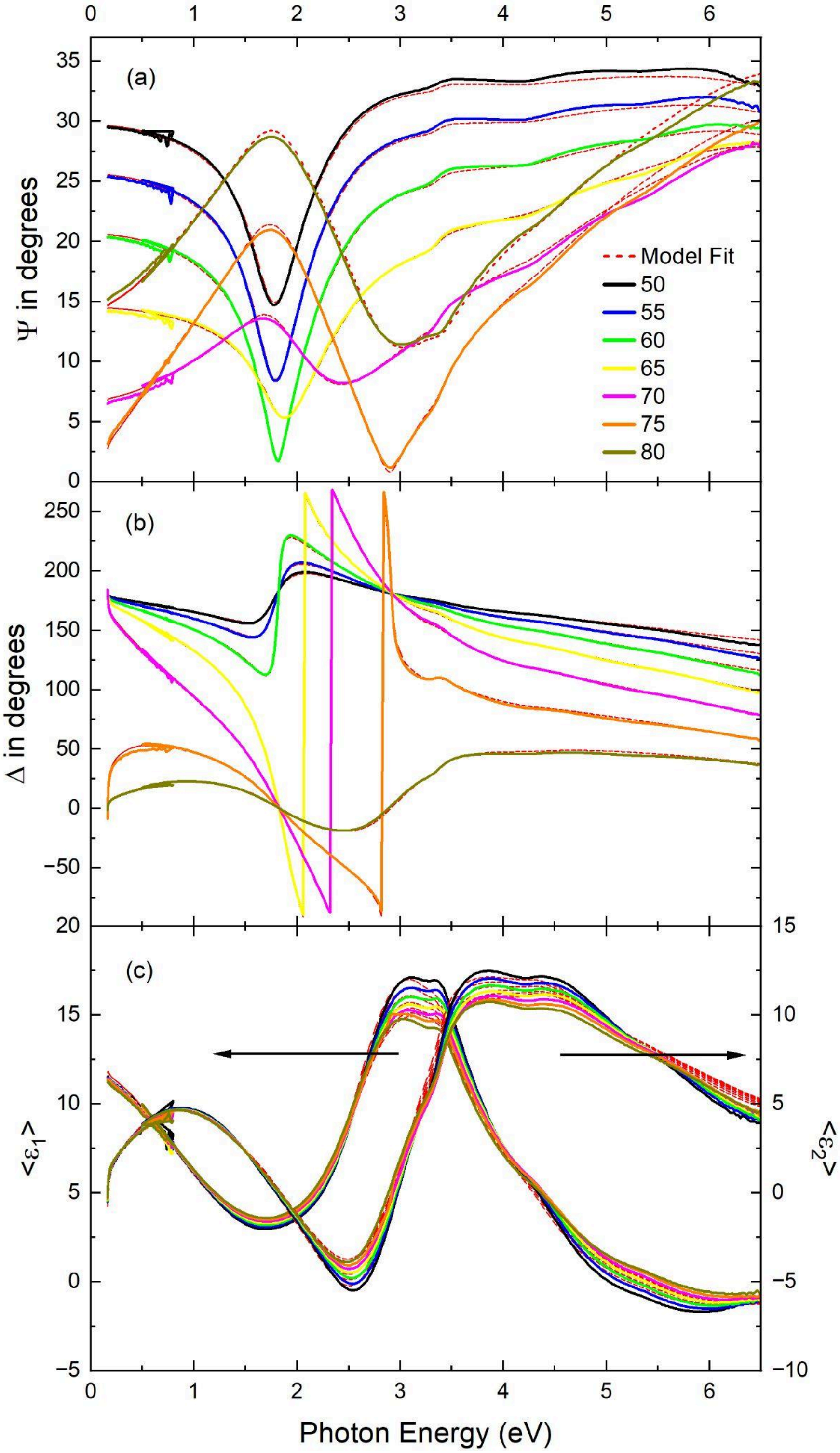

Fig. 17: Ellipsometric angles (a) Ψ and (b) Δ versus photon energy (symbols: data, lines: model) at different incident angles at room temperature for a 23 nm TaN layer on a Si substrate with a 45 nm thick thermal oxide (center of wafer). Data from both ellipsometers were merged. (c) The same data is displayed as a pseudodielectric function.

In Fig. 17(c), the IR region with the SiO_2 lattice absorption (approximately between 0 and 0.2 eV) was removed from the graph because it is not relevant to this part of the research since that corresponds to the oxide layer, but it is included in the supplementary material of this thesis.

Using the coupons with only thermal oxide on Si (52 nm thick as-deposited, 43 nm thick after etching to improve adhesion), an SE dispersion model was first developed for the thermal oxide using three Gaussian oscillators at 56, 132, and 146 meV in the infrared spectral region to account for vibrations of the silicon-oxygen bonds and a fixed pole at 11 eV with variable amplitude to model the visible and ultraviolet dispersion. This silicon-oxide model was then incorporated in the analyses of the coupons with a stack of ALD TaN on silicon oxide on bulk Si. The TaN layers were well described with a model that includes one Tauc-Lorentz oscillator with a band gap of about 1.5-1.8 eV, two Gaussians, and one UV pole outside our spectral range to account for transitions into excited electronic states. A Tauc-Lorentz oscillator is the most common approach to describe the optical constants of amorphous insulators such as amorphous Si, silicon nitride, etc [45]. It also works well for our TaN layers. No infrared oscillators were needed to describe the optical response of the TaN layer.

Ellipsometry can sometimes determine multiple thicknesses in a layer stack, especially if the optical constants of each layer are known. That is not the case here, since the TaN optical constants are the goal of our investigation. We use the TaN layer thickness of 23 nm determined by XRR (see below) as an input for our ellipsometry fit. The SiO_2 layer thickness cannot easily be determined from XRR, since SiO_2 and Si have a similar scattering length density. We found that good fits to the ellipsometric angles are possible with a broad range of SiO_2 thicknesses ranging from 35 to 52 nm. We therefore determine the TaN optical constants at room temperature for various SiO_2 thickness scenarios, as shown in Fig. 18(a). An SiO_2 thickness of 44 nm yields an excellent description of the region of infrared Si-O molecular vibrations near 0.15 eV, but it leads to a peak in the dielectric function of TaN near 1.2 eV, in the region of the interference fringe seen in the pseudodielectric function in Fig. 17(c). The magnitude of this peak increases if we assume an SiO_2 thickness of 52 nm. It nearly disappears for a SiO_2 thickness of 35 nm. The magnitude of the main TaN peak around 4 eV depends much less on the SiO_2 thickness. The strong dependence of the peak at 1.2 eV on the SiO_2 thickness in our fit is suspicious. Most likely, this peak is an artifact that stems from an incomplete removal of interference effects. Since this peak disappears if we assume an SiO_2 thickness of 35 nm, a SiO_2 thickness of 35 nm is the most likely scenario and we fix it in our subsequent analysis work.

The dielectric function of TaN at room temperature resulting from the fit (with an SiO_2 thickness of 35 nm) is shown in Fig. 18.

To study the temperature dependence of the dielectric function of TaN, we performed infrared ellipsometry measurements (from 0.03 to 0.7 eV) at 80 K, 190 K, and 300 K as well as visible/UV ellipsometry measurements (from 0.5 eV to 5.5 eV) at 80 K, 190 K, 300 K, 400 K, 500 K, and 600 K at a single angle of incidence (70°) in a UHV cryostat. The angle of incidence is limited to 70° by the orientation of the cryostat entrance and exit windows. Because of reflection losses at these windows and other experimental reasons, the spectral range in the UV was more limited for measurements inside the cryostat than in air. For the analysis of the resulting ellipsometric angles, the temperature dependence of the dielectric function of bulk Si was taken into account based on the data of Franta et al. [46, 47].

Fig. 18(a) below shows the dielectric functions of 23 nm TaN evaluated for different assumptions of the SiO_2 layer thickness. The assumption for the oxide thickness that works the best with our data is 35 nm, and this can be concluded especially because we notice that the 35 nm ε_2 component plot is the only curve not showing a peak that goes to the infrared range below 2 eV, which could only be explained as artifacts in our experimentally obtained data. Also shown in Fig. 18(b), the temperature dependence of the dielectric function of TaN is small. The band gap of TaN (more precisely, the Tauc gap extracted from our Tauc-Lorentz oscillator model) decreases from 1.8 eV at 80 K to 1.5 eV at 600 K. A similar decrease of the band gap with increasing temperature is seen for other materials [35]. Furthermore, as expected, the broadening of the main peak around 3.5 eV increases with increasing temperature [35], associated with small changes in the high-frequency dielectric constant at 0.5 eV. The imaginary part of ε remains small at all temperatures, indicative of the insulating properties of the TaN layer.

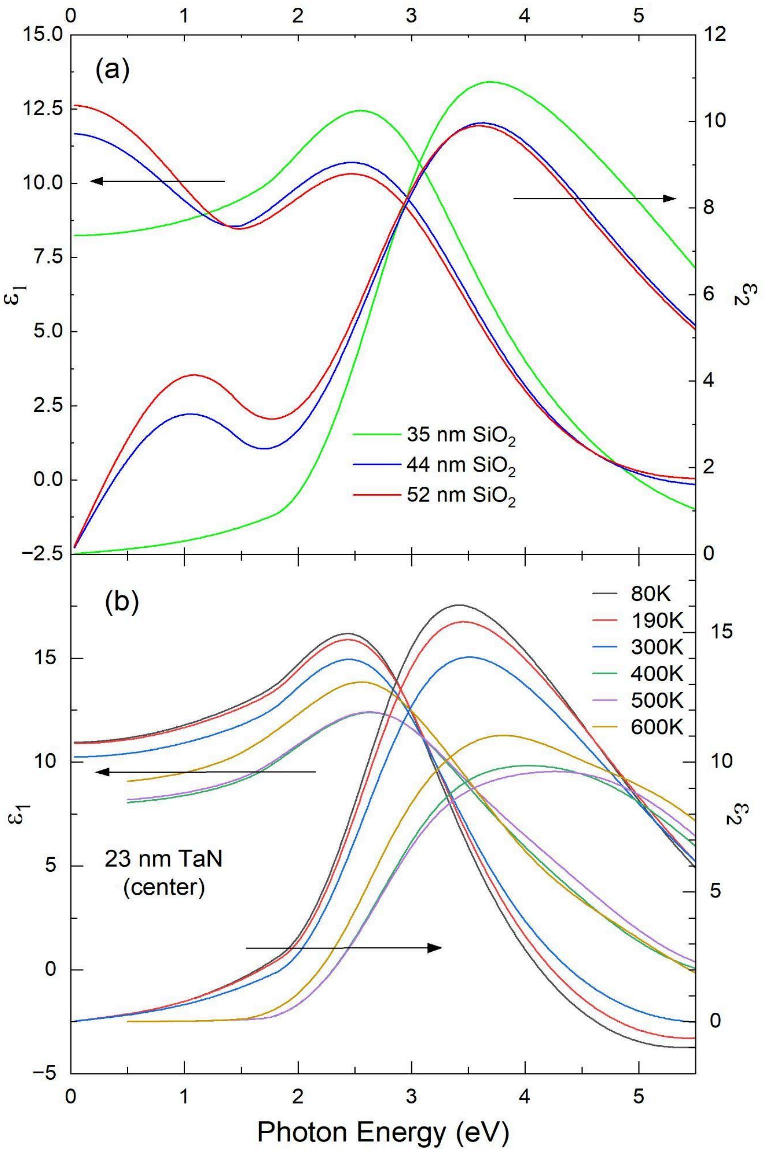

Fig. 18: (a) Real (left) and imaginary (right) parts of the dielectric function of a 23 nm thick TaN layer evaluated for different assumptions of the SiO_2 thickness: 52 nm (red), 44 nm (blue), and 35 nm (green). (b) Real and imaginary part of the dielectric function of a 23 nm ALD TaN film versus photon energy using data acquired at 70° at different temperatures from 80 K to 600 K, assuming an SiO_2 thickness of 35 nm.

Fig. 19 below shows the dielectric functions of TaN surface layers for wafers with the thickness of 23 nm and 13 nm. The dielectric functions of both follow the same overall pattern in relation to the photon energy, which is expected since they both are the same material, but the values for the real and imaginary components of the dielectric function appear smaller with the thinner sample.

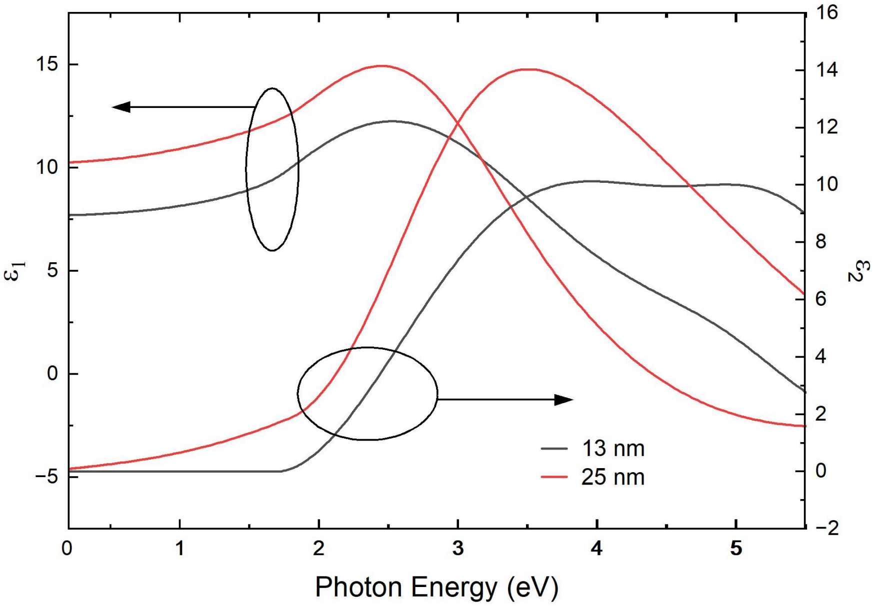

Fig. 19: Real and imaginary parts of the dielectric function of the 13 nm and 23 nm thick TaN layers.

According to the Beer-Lambert law, the decrease in the intensity of light, I, as it passes through a medium is an exponential function of the distance, d, it travels [50]:

$$I = I_o e^{-\alpha d} \tag{22}$$

where I_o is the initial light intensity entering the sample, I is the transmitted light intensity after passing through the sample, e is the base of the natural logarithm, α is the absorption coefficient of the medium, and d is the path length or thickness of the sample. By rearranging the exponential form we can derive the logarithmic form of the Beer-Lambert law.

$$A = ln(\frac{I_o}{I}) = \alpha d \tag{23}$$

A is the absorbance, which is a unitless value derived from the ratio of the initial intensity to the transmitted light intensity, basically it represents how much light the material absorbs at a specific wavelength [50].

This law can give us an explanation for why the dielectric function of the thinner sample is different than that of the thicker sample. Because the thinner sample's film thickness is approximately half of the thicker sample, the absorbance was also halved while the absorption coefficient remained the same. Another explanation could be that the 13 nm sample could be almost completely oxidized forming some type of Ta_xO_x which made its absorption coefficient different, therefore, changing its dielectric functions. Another explanation could come from excitonic enhancement, which is where excitons, bound states of electrons and holes, significantly modify a material's optical properties, like the absorption coefficient, due to the attractive Coulomb interaction between the electron and hole. This could explain why the thin and thick films have different absorptions. Something similar is shown in Fig. 20, where samples of different thicknesses of ZnO/SiO_2 were measured using SE, and their optical constants followed a similar path but with much different absorptions for the real and imaginary parts of their dielectric constants [51].

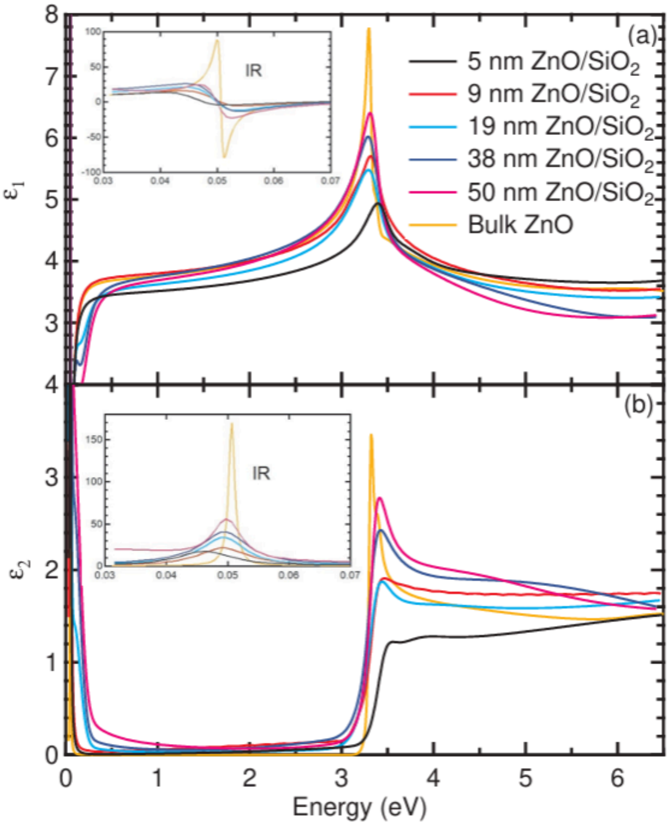

Fig. 20: Real and imaginary parts of the complex dielectric function for ZnO films on SiO_2 versus photon energy. Image retrieved from [51].

So far the measurements were focused mostly on the center coupon of the 300 mm wafer, but sections were taken from the middle and edge parts as well to ensure uniformity in thickness and optical constants of the TaN layer throughout the entire wafer. Fig. 21 below shows the optical constants measured for these three sections on each of the two 300 mm wafers with different TaN nominal thicknesses, 12 nm and 24 nm. The imaginary part of the dielectric function of the three sections in both graphs shows a band gap near 1.7 eV at room temperature, which confirms the desired objective of maintaining uniform optical constants throughout the wafer. Also, there are peaks in the IR region for most plots in both graphs. Since these two graphs were made using a TaN model on top of an SiO_2 model that considered a thickness of 40 nm instead of 35 nm, it is possible these peaks are due to an artifact caused by an incomplete removal of the interference fringe.

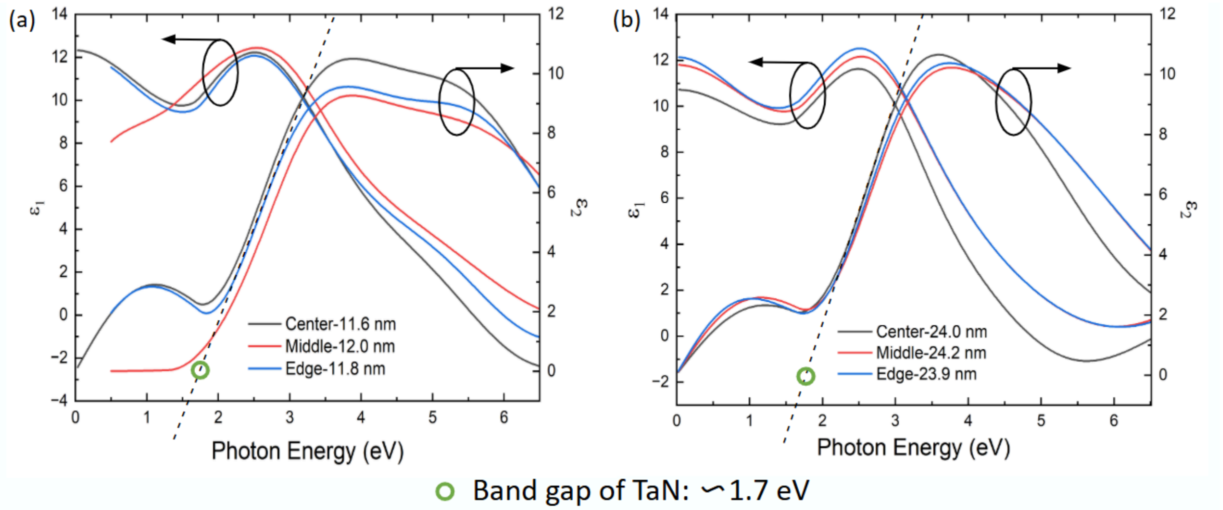

Fig. 21: Optical constants of the center, middle, and edge sections of the 300 mm wafers (a) for the 12 nm TaN layer, and (b) for the 24 nm TaN layer.

Fig. 22(a) shows a nearly linear relationship between the number of ALD cycles and the thickness of ALD TaN for thickness values from 1 nm to 23 nm. Fig. 22(b) present TEM images that show the ALD TaN, confirming the thickness as 25 nm. The SiO_2/TaN interface in Fig. 22(b) is clean with no signature of an interfacial layer.

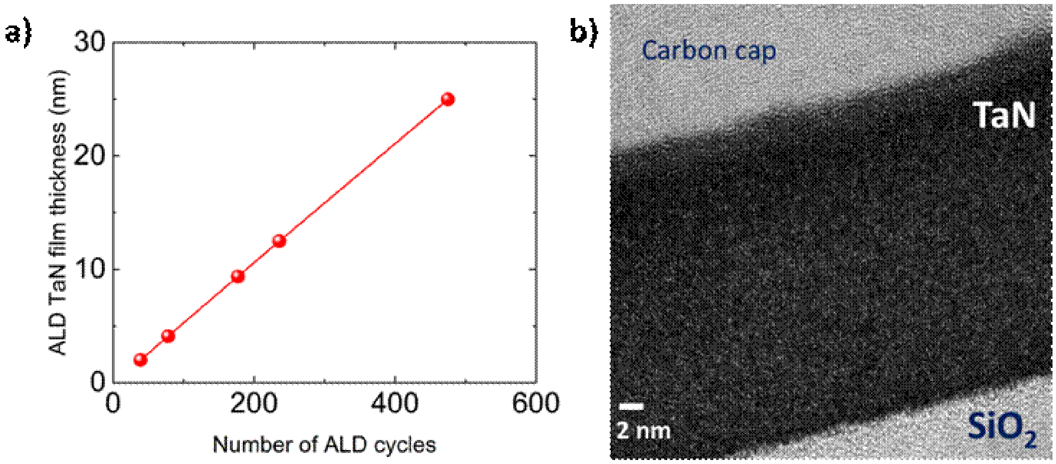

Fig. 22: Film stack and process development for ALD TaN film: a) ALD TaN thickness versus number of ALD cycles, b) TEM image showing ALD TaN film and interfaces.

XRR modeling was done using a stack of Si/thermal oxide/ALD TaN with a proprietary genetic algorithm that permitted the density and thicknesses of the different films to be varied within specified limits to optimize the fit. Fig. 23 shows the results of XRR analysis for thickness determination at different locations on the wafer spanning from the wafer center to the wafer edge for two different thicknesses of ALD TaN. The within-wafer thickness non-uniformity (standard deviation as a percentage of median) is less than 1% for 23 nm ALD TaN and ~1.1% for 13 nm ALD TaN. The variation of the extracted XRR thickness as a function of (X, Y) coordinates on the wafer is shown in Fig. 23(a). Figs. 23(b) and 23(c) show the XRR raw data and fit for the 13 nm and 23 nm ALD TaN thicknesses at wafer mid radius (0 mm, 70 mm). The thickness results from XRR data modeling are consistent with the thickness values obtained from the TEM cross-sections and from ellipsometry.

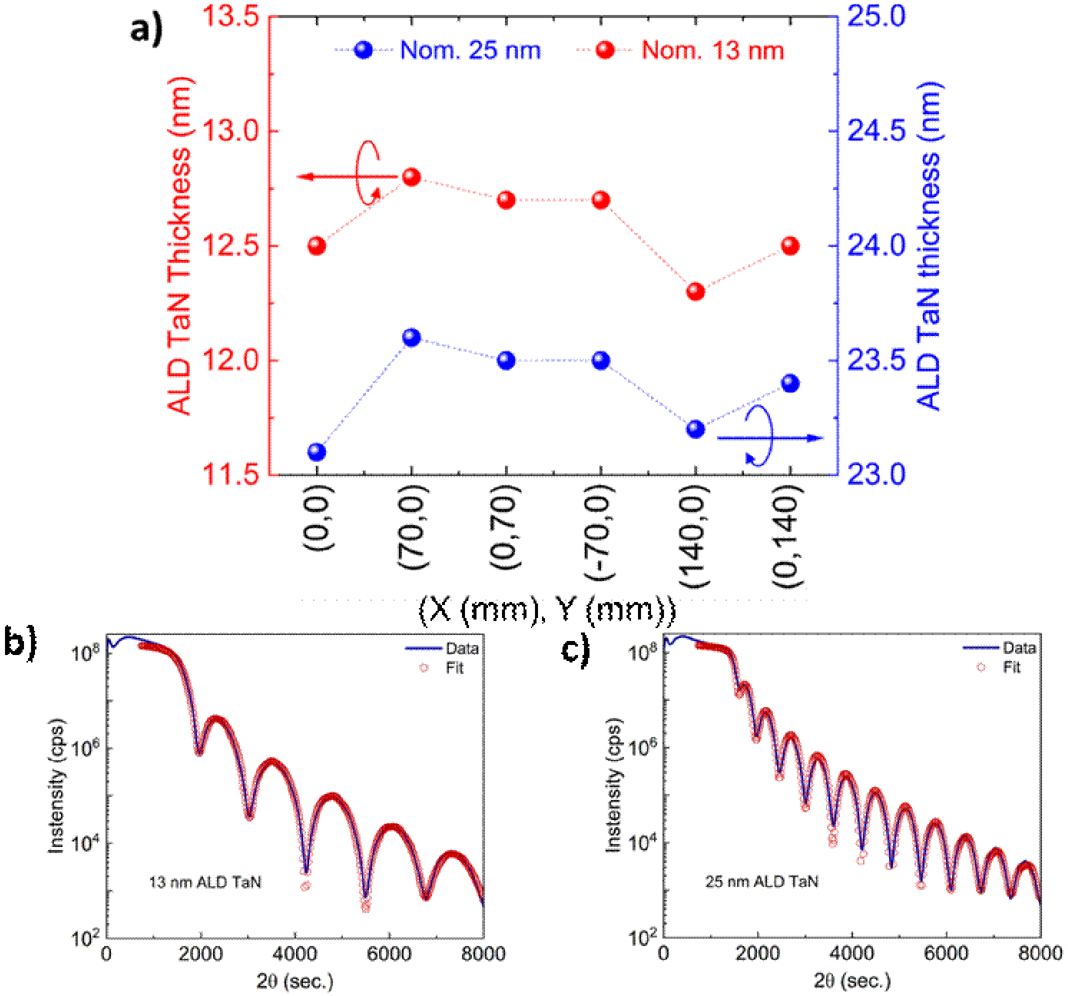

Fig. 23: Thickness determination from XRR across the 300 mm wafer: a) thickness as a function of location (X, Y) on the wafer for both nominal thicknesses, b) Example fit for XRR data for 13 nm ALD TaN wafer at (0 mm, 70 mm), c) example fit for XRR data for 25 (23) nm ALD TaN wafer at (0 mm, 70 mm).

Fig. 24 shows the AFM traces of the 25 nm (23 nm) ALD TaN film at different locations across the 300 mm wafer. The roughness values are <0.5 nm at all the points on the wafer, consistent with the roughness values extracted from the XRR measurements. This roughness (as well as the thickness of the native oxide on TaN) was small and could be ignored in the ellipsometry analysis.

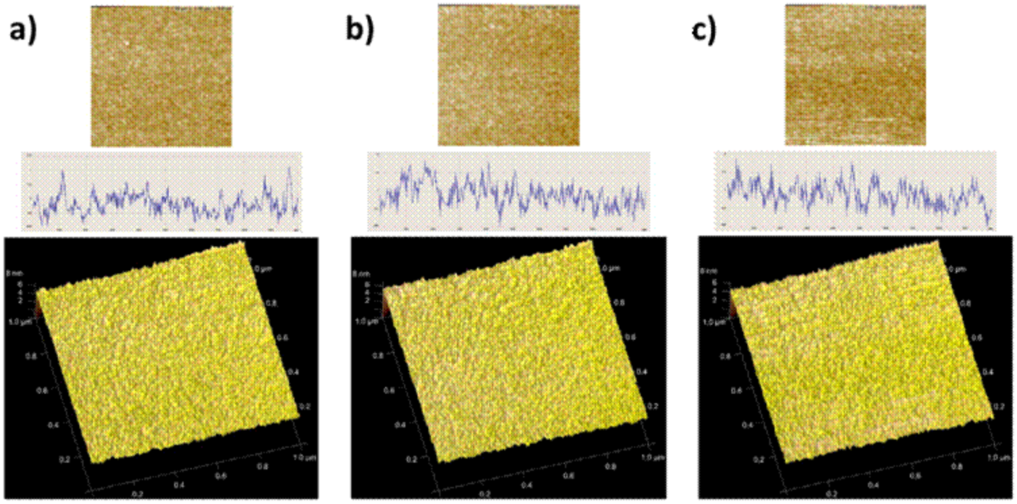

Fig. 24: AFM of 25 (23) nm ALD TaN film at a) wafer center, b) wafer mid radius (0 mm, 75 mm), c) wafer edge (0 mm, 140 mm). In each case, the top picture shows the 2D scan, the middle picture shows the line scan (topography versus scan length), and the bottom picture shows the 3D AFM scan.

Fig. 25 shows the selected area diffraction (SAD) using the 300 keV TEM beam for the ALD TaN film and Si substrate. The diffraction spots in the SAD of TaN (Fig. 25(a)) show the crystalline structure of Ta_5N_6 [48]. The two-fold symmetry observed in the SAD pattern is consistent with the hexagonal structure observed from the (110) zone axis. This crystal symmetry was confirmed at multiple locations on samples taken from the center and edge of the wafer—two examples are shown in Fig. 25(a,b). We determined the value of lattice constant to be 5.25 Å from these SAD patterns of ALD TaN. In Fig. 25(b), we confirmed that the SAD for Si substrate is ascribable to (110) zone, as expected.

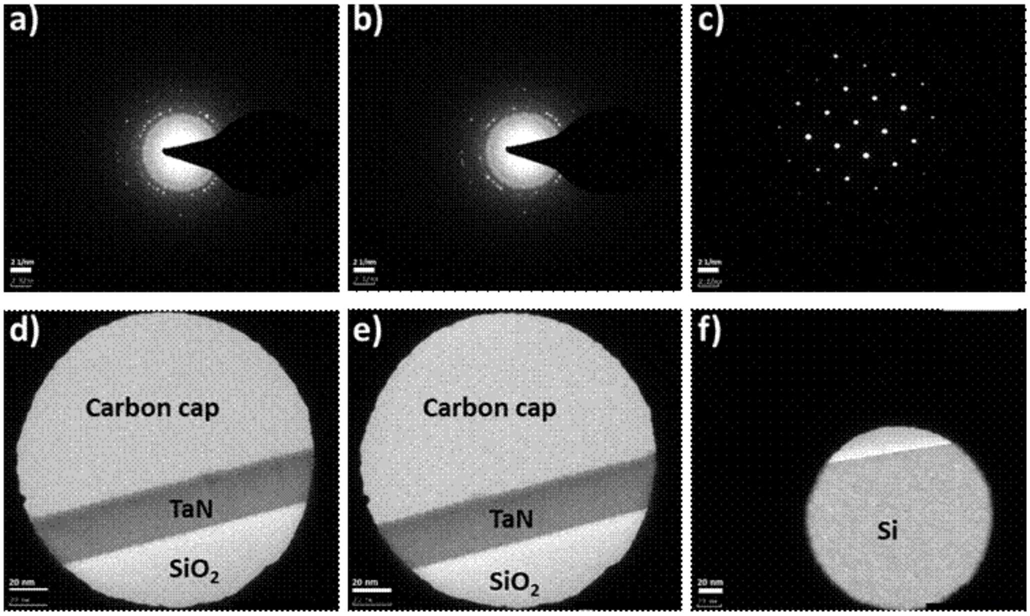

Fig. 25: Selected area diffraction (SAD) using TEM for different layers. SAD for (a) only ALD TaN from wafer center, (b) ALD TaN from a different location on TEM lamella taken from wafer center, (c) Only Si substrate, The corresponding TEM images with aperture sizes are shown in (d), (e), and (f).

If a thin layer (like our TaN) is mostly amorphous, but contains a few crystalline regions, then only the crystalline regions will be seen in XRD or SAD. On the other hand, the amorphous regions will dominate the ellipsometry spectra (which can be modeled using a Tauc-Lorentz oscillator model for amorphous materials). Therefore, the presence of diffraction spots in our TaN layer is not necessarily in conflict with the use of an optical dispersion model for an amorphous material. A fully crystalline (or poly-crystalline) material is likely to show several sharp features in the optical constants.

Fig. 26 shows the in-plane and out-of-plane XRD data of Si/SiO_2/ALD TaN and Si/SiO_2. After eliminating the peaks associated with Si/SiO_2, there is a broad peak associated with ALD TaN with a 2θ value of 33.86°, and the lattice constant value of 5.27 Å for a, which is consistent with the JCPDS database for hexagonal TaN with a card number 00-153-9256. However, it is not possible to determine the 'c' value of lattice constant based on just one broad XRD peak, and this difficulty with making a definitive assignment of specific phase has also been seen in previous literature for Si/SiO_2/ALD TaN [39]. XRD analysis supports the Ta_5N_6 hexagonal structure (as determined by SAD) for the ALD TaN films deposited on Si/SiO_2.

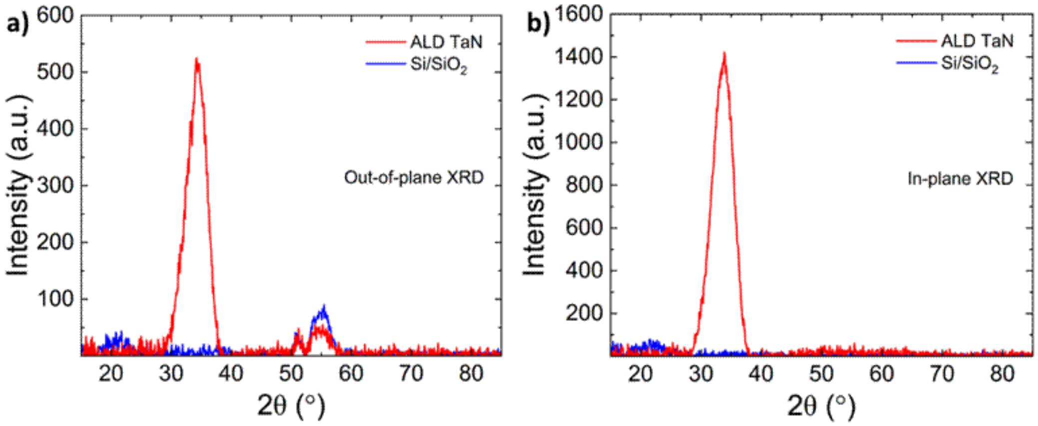

Fig. 26: XRD of ALD TaN versus Si/SiO_2: a) in-plane XRD, b) out-of-plane XRD

Fig. 27 shows the TEM images with a zoomed-in view of ALD TaN, SiO_2/ALD TaN interface, and Si/SiO_2 interface. Fig. 27(a) shows a high-magnification image of the TaN film. The Si/SiO_2 interface in Fig. 27(b) is clean and shows the crystalline lattice of Si.

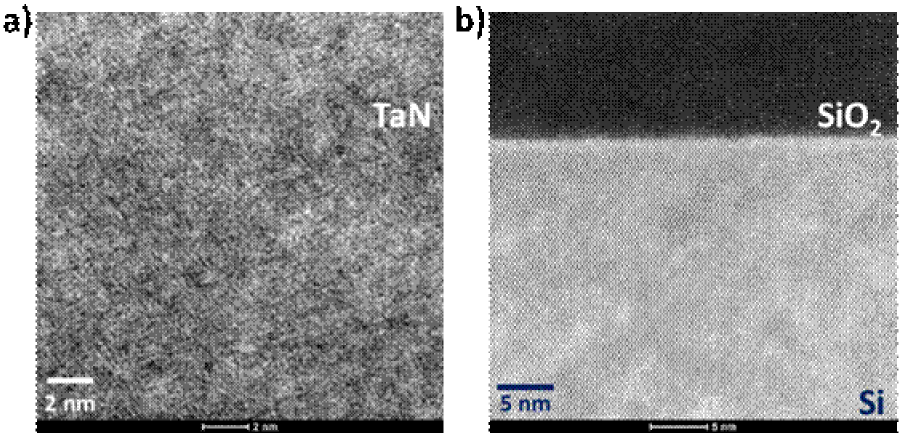

Fig. 27: TEM image showing the zoomed-in view of a) ALD TaN, b) Si/SiO_2 interface.

Fig. 28 shows the sputterXPS analysis using CasaXPS for 23 nm ALD TaN films measured for coupons from the wafer center for different sputter times and depths from the surface of TaN. We focus on the Ta4f, O1s, C1s, Ta4p, and N1s regions for XPS analysis. We used the Shirley-type background in CasaXPS software for background subtraction. The peaks were fitted using Gaussian/Lorentzian product line shapes [40-42]. The Ta4p and N1s peaks were fitted as per the XPS guidelines from the earlier literature, and inelastic mean free path (IMFP) calculations were taken into account to get the corrected area for Ta4p and N1s in order to determine the N/Ta ratio [41, 42]. The N/Ta ratio is ~1.2 at all the depths inside the TaN as determined by calculating the ratio of the corrected total area under the curve from the Ta4f peak to the corrected total area of the N1s peak after fitting using CasaXPS. It is important to note that there were no detectable amounts of carbon and oxygen seen by XPS deeper into the ALD TaN film. The O1s peak also indicates the presence of hydrocarbon bonded to oxygen [43], which we ascribe to surface hydrocarbons. The N1s peak position (395.99 eV) and Ta4p peak position (403.38 eV) are consistent with the literature. XPS spectra for coupons from different locations on the wafer overlap with each other, showing a good across-wafer non-uniformity for TaN composition.

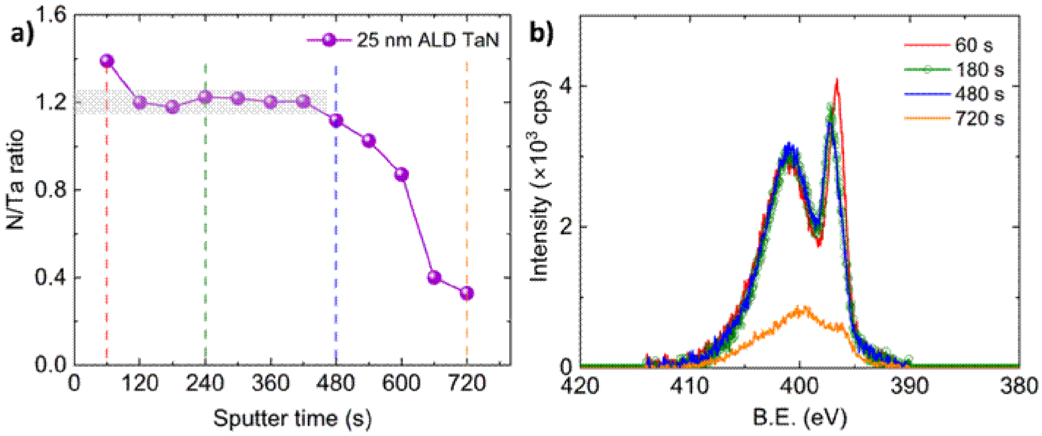

Fig. 28: Extracted N/Ta ratios as a function of sputter time from sputterXPS, b) XPS data at different sputter times shown by dashed lines in (a)

4.4 Conclusion

In this study, we explored the deposition and characterization of ALD TaN films for their application as tunnel barriers in Josephson junctions for superconducting quantum circuits. XRR, TEM, XPS, SE, and AFM measurements showed good across-wafer uniformity of the thickness, composition, roughness, and optical characteristics of ALD TaN films across 300 mm wafers. The bandgap of the ALD TaN is 1.5-1.8 eV, with no evidence for free-carrier absorption in the infrared region, consistent with the insulating nature of the ALD TaN film. The XRD and SAD analysis indicated Ta_5N_6 hexagonal structure. The sputter XPS results show the N/Ta ratio as 1.2 and the absence of carbon and oxygen in the film. These characteristics demonstrate the suitability of ALD TaN for integration into Josephson junctions for use in quantum computing and superconducting logic circuits.

The ALD TaN band gap was determined to be 1.5-1.8 eV, showing a very small change in the imaginary part of the dielectric function around 1 eV when exposed to different temperatures. This demonstrates its advantages over traditional aluminum oxide barriers of higher band gap used in tunnel barriers. The smaller barrier height allows for thicker films to be utilized for the same magnitude of Josephson tunneling current, improving process control margin. The excellent surface roughness and band gap uniformity across the 300 mm wafer illustrate ALD TaN as a potential material for Josephson junctions to achieve thermally stable, reliable, and repeatable superconducting qubit devices.

Future work will focus on the determination of dielectric loss in ALD TaN and its integration as tunnel barriers into Josephson junctions and the determination of coherence times of superconducting qubit devices made from these Josephson junctions.

4.5 Author Contributions

E. Bhatia: Writing (lead). **A. Lopez Gonzalez:** Data acquisition (equal); Formal analysis (equal); Visualization (equal); Writing (supporting). **S. Rao:** Project administration (equal); Supervision (equal); Funding acquisition (equal); Writing - review & editing (equal). **S. Zollner:** Project administration (equal); Supervision (equal); Funding acquisition (equal); Writing - review & editing (equal).

4.6 Supplementary material

Temperature-Dependent Dielectric Function of Tantalum Nitride Formed by Atomic Layer Deposition for Tunnel Barriers in Josephson Junctions

Ekta Bhatia,[1] Aaron Lopez Gonzalez,[2] Yoshitha Hettige,[2] Sandra Schujman,[1] Kevin Musick,[1] Thomas Murray,[1] Kim Kisslinger,[3] Mingzhao Liu,[3] Satyavolu Papa Rao,[1] and Stefan Zollner[2]

[1]*NY CREATES, Albany, NY, USA*

[2]*Department of Physics, New Mexico State University, Las Cruces, NM, USA*

[3]*Brookhaven National Laboratory, Upton, NY*

The supplementary material shows raw ellipsometry data, which were summarized and discussed in the main article.

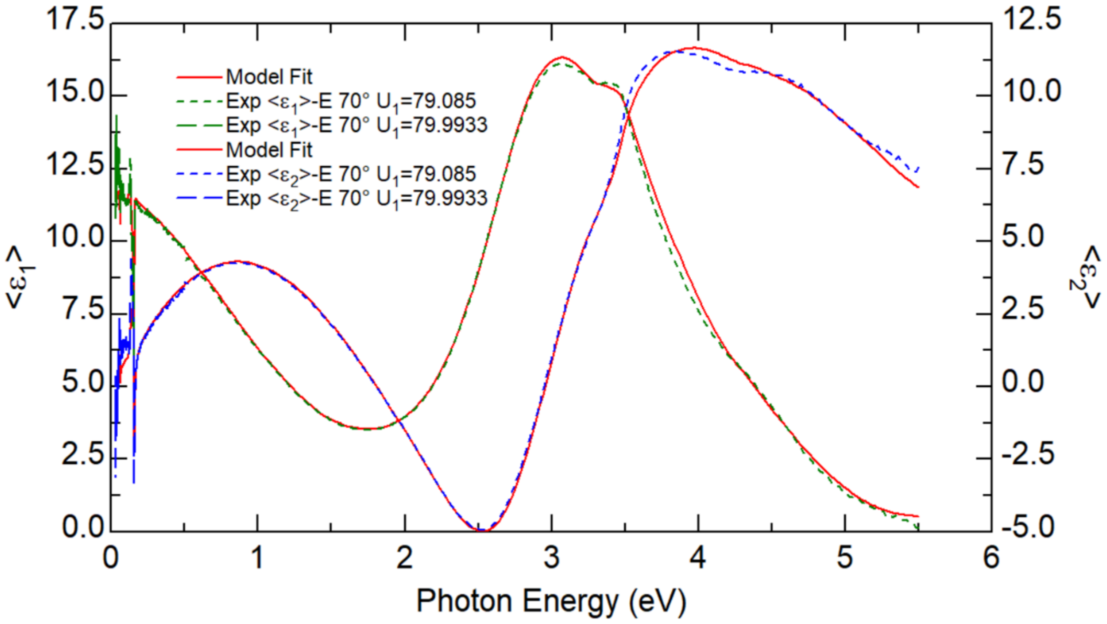

Fig. S1: Real and imaginary part of the pseudodielectric function for 23 nm of TaN and 35 nm of SiO_2 at 80 K (symbols: data; lines: fit).

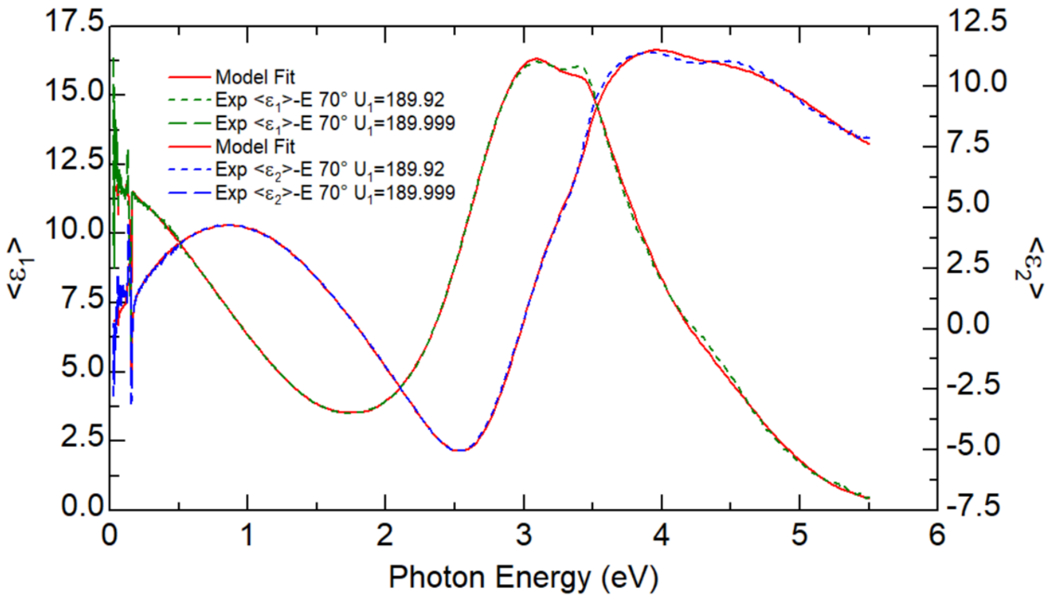

Fig. S2: Real and imaginary part of the pseudodielectric function for 23 nm of TaN and 35 nm of SiO_2 at 190 K (symbols: data; lines: fit).

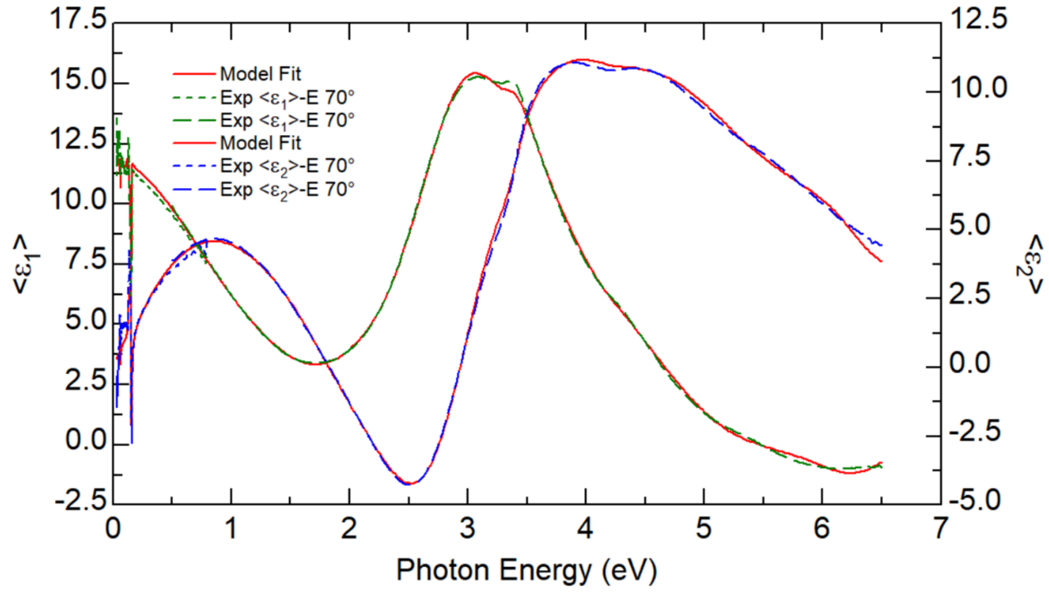

Fig. S3: Real and imaginary part of the pseudodielectric function for 23 nm of TaN and 35 nm of SiO_2 at 300 K (symbols: data; lines: fit).

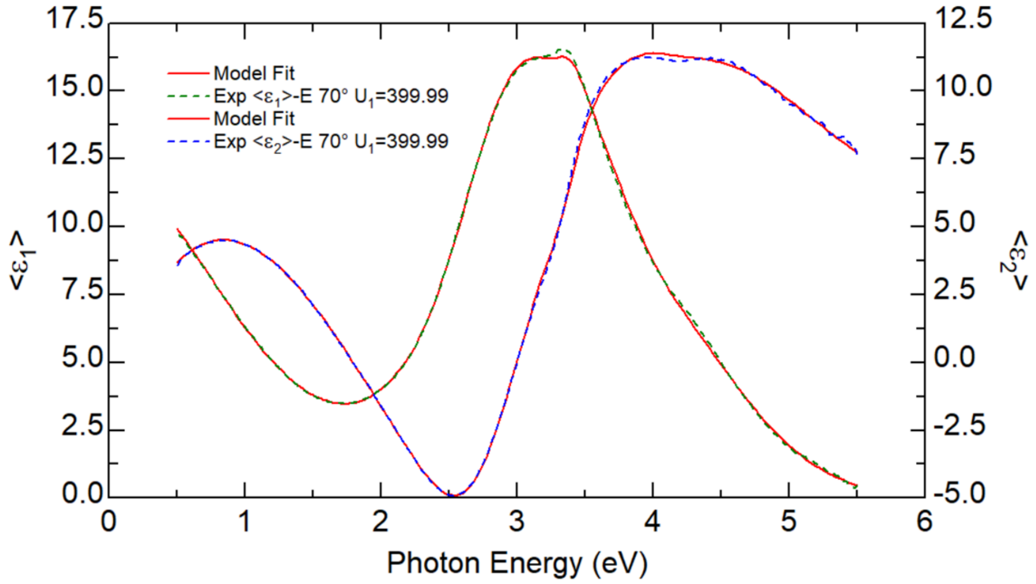

Fig. S4: Real and imaginary part of the pseudodielectric function for 23 nm of TaN and 35 nm of SiO_2 at 400 K (symbols: data; lines: fit).

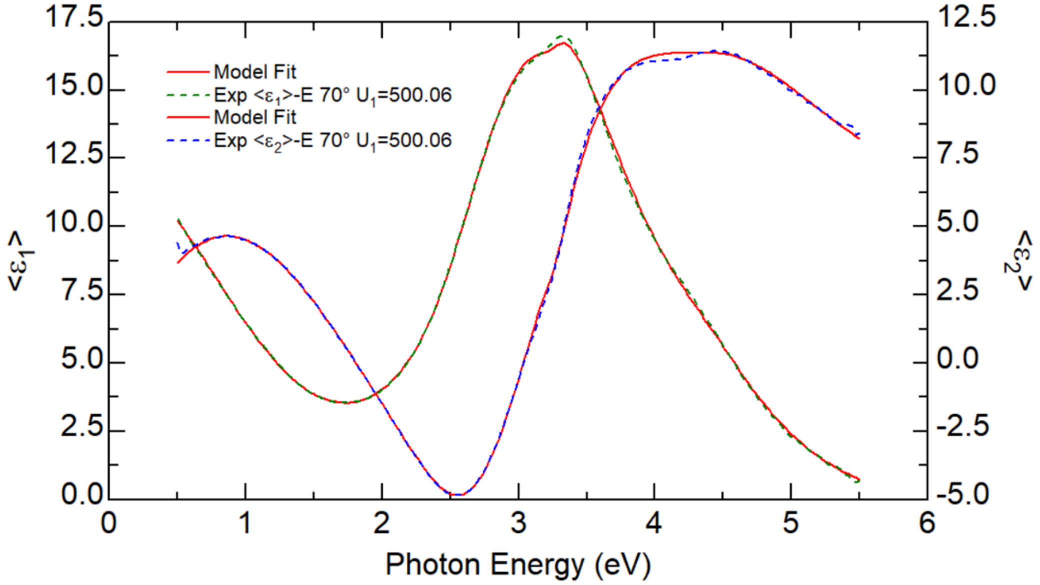

Fig. S5: Real and imaginary part of the pseudodielectric function for 23 nm of TaN and 35 nm of SiO_2 at 500 K (symbols: data; lines: fit).

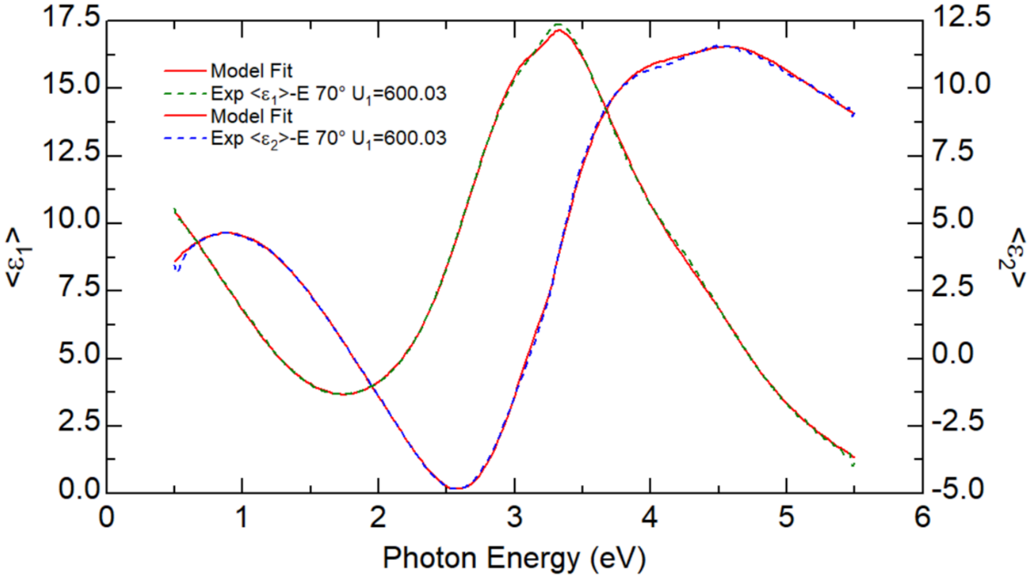

Fig. S6: Real and imaginary part of the pseudodielectric function for 23 nm of TaN and 35 nm of SiO_2 at 600 K (symbols: data; lines: fit).

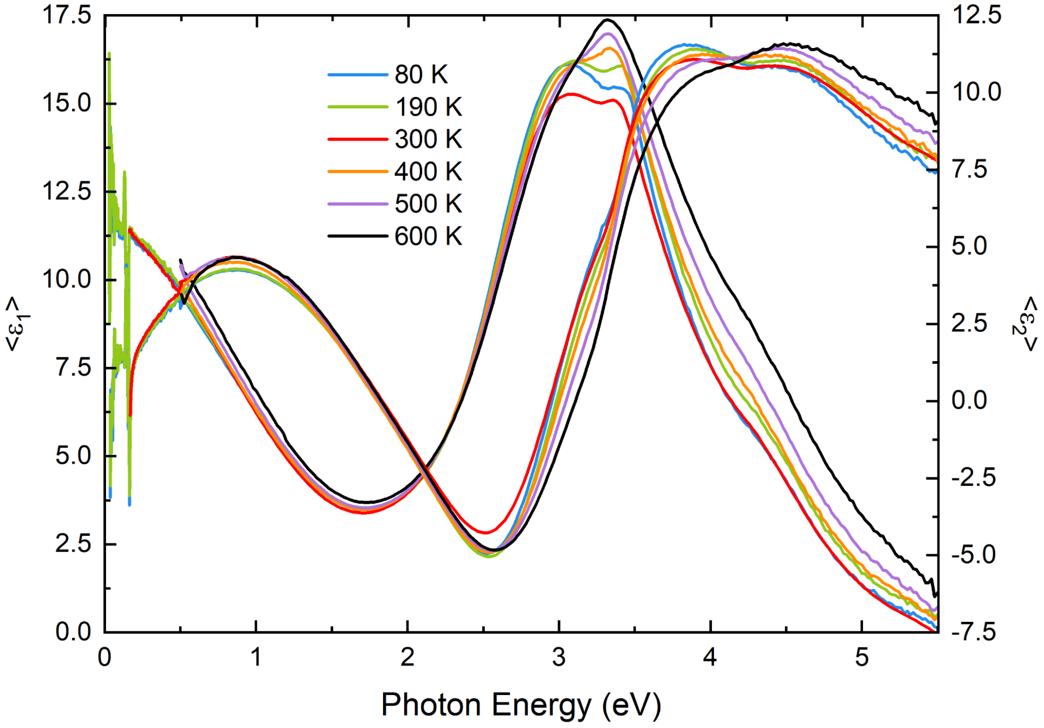

Fig. S7: Real and imaginary parts of the pseudodielectric function for 23 nm of TaN and 35 nm of SiO_2 from 80 K to 600 K (only experimental data are shown).

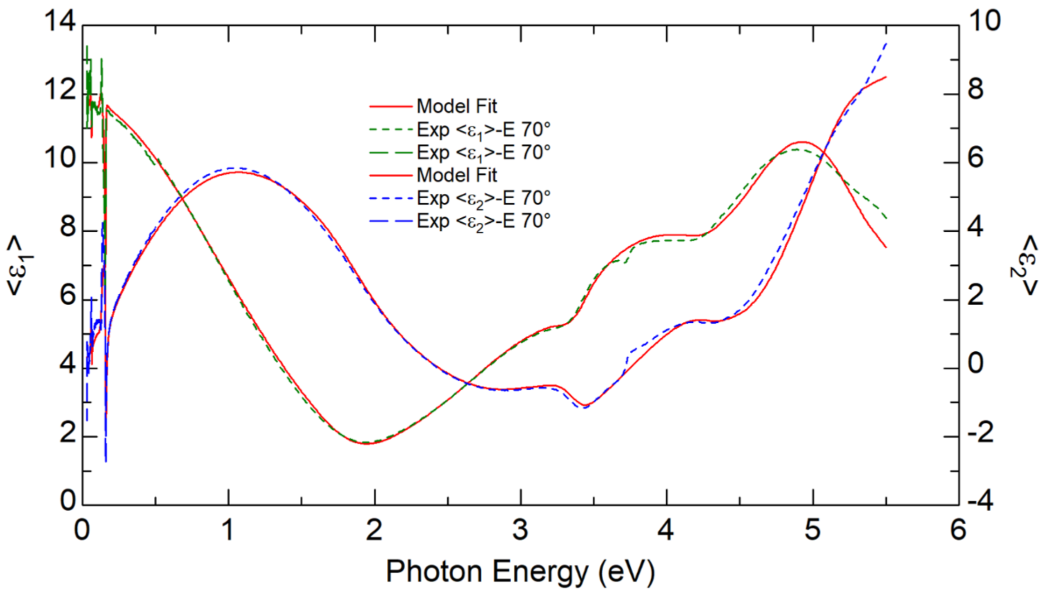

Fig. S8: Real and imaginary part of the pseudodielectric function for 13 nm of TaN and 35 nm of SiO_2 at 300 K (symbols: data; lines: fit).

5 OUTLOOK AND SUMMARY

The objective of this research was to investigate the temperature dependence of the optical constants of tantalum nitride (TaN) thin films deposited by atomic layer deposition (ALD) on 300 mm silicon wafers with a silicon dioxide interlayer. The goal of the overall project was to determine whether ALD TaN exhibits the dielectric and structural characteristics suitable for use as an insulating tunnel barrier in superconducting quantum devices, specifically Josephson junctions. This thesis focused on the spectroscopic ellipsometry research done for this project.

The theoretical foundation, presented in the theory section, highlighted the importance of optical constants as manifestations of a material's electronic band structure. Spectroscopic ellipsometry was emphasized as a precise, non-destructive method for determining the refractive index *n*, extinction coefficient *k*, and dielectric function ε across a wide spectral and temperature range. Using advanced instruments, namely the J.A. Woollam IR-VASE and VASE ellipsometers coupled with a Janis ST-400 ultrahigh-vacuum cryostat, measurements were performed from 0.03 to 6.5 eV and over temperatures from 80 K to 600 K. Theoretical models such as Tauc-Lorentz and Gaussian oscillators were applied to describe the optical dispersion of TaN and its response to temperature changes.

Complementary XRR measurements, discussed in the next section, provided precise quantification of layer thickness, density, and surface roughness. The XRR data modeled using PANalytical's Empyrean diffractometer confirmed a TaN thickness of approximately 23.5 nm, an oxide layer thickness of 39.7 nm, and a TaN density of 9.78 g/cm³, closely matching theoretical and ellipsometric values, and with only small deviations from the results calculated directly from the experimental data. The excellent agreement between experimental data and modeled results demonstrated the reliability of the deposition and characterization methods. Minor discrepancies in mid-range intensity between experimental and modeled XRR curves were attributed to subtle density gradients or interface effects, but overall, the ALD process produced uniform and repeatable thin films.

The last section presented the main experimental findings on the temperature-dependent dielectric function of ALD TaN. The ellipsometry results revealed that TaN films with nominal thicknesses of 13 nm and 23 nm exhibit insulating characteristics across the investigated temperature range. No evidence of free-carrier absorption was observed in the infrared region, confirming the dielectric nature of these films. The band gap extracted from the Tauc-Lorentz model varied between 1.5 eV and 1.8 eV, showing a modest decrease with increasing temperature, consistent with the expected band-gap narrowing effect observed in many semiconductors and insulators. This value is smaller than the band gap of Al_2O_3, implying that ALD TaN could enable thicker, more controllable tunnel barriers while maintaining desired current densities in Josephson junctions. The dielectric function of ALD TaN showed minimal variation with temperature, indicating excellent thermal stability, a desirable feature for integration into superconducting circuits.

In conclusion, this work successfully characterized the optical and structural properties of ALD TaN thin films across temperature and wafer scale. The films exhibit a stable, uniform, and insulating dielectric behavior with a moderate band gap and excellent thermal robustness. These characteristics validate ALD TaN as a promising alternative to aluminum oxide barriers in Josephson junctions, potentially enabling thicker, more stable tunnel barriers with enhanced reproducibility in superconducting quantum circuits. The combination of low surface roughness and high uniformity positions ALD TaN as a strong candidate for integration into scalable quantum computing architectures. Future research should focus on the study of defect-related states within the band gap and the fabrication of complete Josephson junction devices incorporating ALD TaN barriers to evaluate their performance in superconducting qubits. Through these next steps, the findings of this thesis can bridge the gap between material characterization and device-level implementation, advancing the development of high-coherence superconducting quantum technologies.

REFERENCES

[1] I. Kaplan, *The Pauli exclusion principle: origin, verifications, and applications* (John Wiley & Sons, Chichester, 2017) pp. 25, 27.

[2] M.H. Saleh, *Study of Structural, Optical and Electrical Properties of PbI_2 Thin Films Prepared by Flash–Evaporation Technique*, Ph. D. thesis, University of Jordan, (2011).

[3] J. Gusakova, B.K. Tay, and V. Gusakov, Phys. Status Solidi **A**, 1–4 (2016).

[4] W. Tausendfreund, J. Phys. C: Solid State Phys, **8** (7), 1000-1009 (1975).

[5] A.R. Forouhi, I. Bloomer, Handbook of Optical Constants of Solid, **2**, 151-175 (1997).

[6] K. Vedam, Thin Solid Films **313–314**, 1–9 (1998).

[7] G.E. Jellison, Thin Solid Films, **234**, 416-422 (1993).

[8] J.A. Woollam, Ellipsometry FAQ, https://www.jawoollam.com, (Accessed July 20, 2025).

[9] H. Fujiwara, *Spectroscopic Ellipsometry: Principles and Applications*, (John Wiley & Sons, Chichester, 2007) pp. 37, 40.

[10] D. Amrani, J. Sci. Educ., **23** (1), 41 (2022).

[11] J.A. Woollam, IR-VASE Mark II Ellipsometer, https://www.jawoollam.com/products/ir-vase-ellipsometer, (Accessed July 21, 2025).

[12] J.A. Woollam, VASE Ellipsometer, https://www.jawoollam.com/products/vase-ellipsometer, (Accessed July 21, 2025).

[13] Lake Shore Cryotronics, ST-400 Series ultra-high vacuum cryostats, https://www.lakeshore.com/products/product-detail/janis/st-400-uhv-cryostat, (Accessed July 22, 2025).

[14] J.A. Woollam, WVASE, https://www.jawoollam.com/ellipsometry-software/wvase, (Accessed July 22, 2025).

[15] E. Chason and T. M. Mayer, Critical Reviews in Solid State and Materials Sciences, **22** (1), 1-67 (1997).

[16] A. Gibaud, M. S. Chebil, and T. Beuvier, “X-Ray Reflectivity”, In G. Bracco and B. Holst (eds), *Surface Science Techniques* (pp. 191-216), Springer, Berlin, Heidelberg, 2013.

[17] A. Gibaud and S. Hazra, Current Science, **78** (12), 1467-1477 (2000).

[18] M. Yasaka, The Rigaku Journal, **26** (2), 1-9 (2010).

[19] J. P. Sauro, J. Bindell, and N. Wainfan, Phys. Rev., **143** (2), 439-443 (1966).

[20] M. R. Sardela, “X-Ray Diffraction and Reflectivity”, In M. Sardela (ed.), *Practical Materials Characterization* (pp. 1-41), Springer Science+Business Media New York, 2014.

[21] Malvern Panalytical, Empyrean, https://www.malvernpanalytical.com/en/products/product-range/empyrean-range/empyrean, (Accessed July 28, 2025).

[22] N. P. de Leon et al., Science **372**, eabb2823 (2021).

[23] Morten Kjaergaard *et al.*, Annual Review of Condensed Matter Physics, **11**, 369–395 (2020).

[24] W. D. Oliver, and P. B. Welander, MRS Bulletin **38**, 816-825 (2013).

[25] G.Wendin and V. S. Shumeiko, Low Temp. Phys., **33**, 724–744 (2007).

[26] J. M. Martinis *et al.*, Physical Review Letters, **95**, 210503 (2005).

[27] A. P. M. Place *et al.*, Nature Communications **12**, 1779 (2021).

[28] C. Wang *et al.*, npj Quantum Information, **8**, 3 (2022).

[29] J. Wilt *et al.*, Physical Review Applied, **7**, 064022 (2017).

[30] E. Bhatia *et al.*, J. Vac. Sci. Technol. B **41**, 033202 (2023).

[31] Q. Xie *et al.*, Applied Surface Science **253**, 1666-1672 (2006).

[32] K. Makise *et al.*, IEEE Transactions on Applied Superconductivity **25**, 1-4 (2014).

[33] M. A. Wolak *et al.*, IEEE Transactions on Applied Superconductivity, **29**, 1-4, (2019).

[34] E. Bhatia *et al.*, Bulletin of the American Physical Society 2024, manuscript in preparation.

[35] S. Zollner *et al.*, Advanced Optical Technologies **11**, 117-135 (2022).

[36] E. Bhatia *et al.*, In *2024 35th Annual SEMI Advanced Semiconductor Manufacturing Conference (ASMC)*, pp. 1-6. IEEE, 2024.

[37] R. A. Carrasco *et al.*, Appl. Phys. Lett. **114**, 062102 (2019).

[38] Y. Y. Wu *et al.* Materials Chemistry and Physics **101**, 269–275 (2007).

[39] H. Kim *et al.* J. Appl. Phys. **92**, 7080–7085 (2002).

[40] J. J. Rumble *et al.* Surf. Interface Anal. **19**, 241–246 (1992).

[41] G. Greczynsk *et al.*, J. Appl. Phys. **132**, 011101 (2022).

[42] Major *et al.*, J. Vac. Sci. Technol. A **38**, 061203 (2020).

[43] J. F. Moulder, Handbook of X-ray Photoelectron Spectroscopy: A Reference Book of Standard Spectra for Identification and Interpretation of XPS Data, page 45 (Physical Electronics, Eden Prairie, MN, 1992).

[44] F. Argall, and A. K. Jonscher. Thin Solid Films **2**, 185-210 (1968).

[45] G. E. Jellison, Jr., and F. A. Modine, Appl. Phys. Lett. 69, 371 (1996); 69, 2137 (1996) (E).

[46] D. Franta, A. Dubroka, C. Wang, A. Giglia, J. Vohánka, P. Franta, and I. Ohlídal, Appl. Surf. Sci. B **421**, 405 (2017).

[47] D. Franta, P. Franta, J. Vohánka, M. Čermák, and I. Ohlídal, J. App. Phys. **123**, 185707 (2018).

[48] Nobuzo Terao, Jpn. J. Appl. Phys. **10** 248 (1971).

[49] H. Fujiwara, *Spectroscopic Ellipsometry: Principles and Applications* (John & Wiley Sons, Chichester, 2007) pp. 158-177.

[50] D. F. Swinehart, J. Chem. Edu. **39** (7), 333-335 (1962).

[51] N. Samarasingha, *Optical characterization of compound semiconductor materials using spectroscopic ellipsometry*, Ph. D. thesis, New Mexico State University, (2021).